Empirical Cross-Calibration of Coherent SWOT Errors Using External References and the Altimetry Constellation

Gerald Dibarboure, Sylvie Labroue, Michael Ablain, Roger Fjørtoft, Alain Mallet, Juliette Lambin, and Jean-Claude Souyris

***Abstract*—This paper gives an overview of an empirical cross-calibration technique developed for the Surface Water Ocean Topography mission (SWOT). The method is here used to detect and to mitigate two spatially coherent errors in SWOT topography data: the baseline roll error whose signature is linear across track, and the baseline length error whose signature is quadratic across track. Assuming that topography data are corrupted by coherent error signatures that we can model, we extract the signatures, and we empirically use the error estimates to correct SWOT data. The cross-calibration is tackled with a two-step scheme. The first step is to get local estimates over cross-calibration zones, and the second step is to perform a global interpolation of local error estimates and to mitigate the error everywhere. Three methods are used to get local error estimates: 1) we remove a static first guess reference such as a digital elevation model, 2) we exploit overlapping diamonds between SWOT swaths, and 3) we exploit overlapping segments with traditional pulse-limited altimetry sensors. Then, the along-track propagation is performed taking the local estimates as an input, and an optimal interpolator (1-D objective analysis) constrained with *a priori* statistical knowledge of the problem. The rationale of this paper is to assume that SWOT's scientific requirements are met on all errors but the ones being cross-calibrated. In other words, the algorithms presented in this paper are not needed at this stage of the mission definition, and they are able to deal with higher error levels (e.g., if hardware constraints are relaxed and replaced by additional ground processing). Even in our most pessimistic theoretical scenarios of baseline roll and baseline length errors (up to 70 cm RMS of uncorrected topography error), the cross-calibration algorithm reduces coherent errors to less than 2 cm (outer edges of the swath). Residual errors are subcentimetric for very low-frequency errors (e.g., orbital revolution). Sensitivity tests highlight the benefits of using additional pulse-limited altimeters and optimal inversion schemes when the problem is more difficult to solve (e.g., wavelengths of less than 1000 km), but also to provide a geographically homogeneous correction that cannot be obtained with SWOT's sampling alone.**

***Index Terms*—Altimetry, calibration, interferometry, remote sensing.**

Manuscript received March 3, 2011; revised August 12, 2011; accepted September 25, 2011. Date of publication November 25, 2011; date of current version May 16, 2012.

G. Dibarboure, S. Labroue, and M. Ablain are with the CLS Space Oceanography Division, 31520 Ramonville St-Agne, France (e-mail: gerald.dibarboure@cls.fr; sylvie.labroue@cls.fr; mablain@cls.fr).

R. Fjørtoft, A. Mallet, J. Lambin, and J.-C. Souyris are with the Centre National d'Etudes Spatiales (CNES), 31401 Toulouse, France (e-mail: roger.fjortoft@cnes.fr; Alain.Mallet@cnes.fr; juliette.lambin@cnes.fr; jean-claude.souyris@cnes.fr).

Color versions of one or more of the figures in this paper are available online at http://ieeexplore.ieee.org.

Digital Object Identifier 10.1109/TGRS.2011.2171976

I. Introduction and Context

A. Paper Overview

The purpose of Section I is to introduce the context and the objectives of this paper, i.e., to give a short description of Surface Water Ocean Topography (SWOT) and the errors tackled by this paper. Section II gives an overview of the cross-calibration methods used. These methods use a two-step approach: 1) to compute local error estimates from the so-called direct and cross-over methods (detailed in Section III) and 2) to perform a global propagation everywhere and for each time step (detailed in Section IV). Section V gives the end-to-end simulation results on the "baseline roll" and "baseline length" errors. Lastly, Section VI expands on these simulations with more general cross-calibration findings and considerations (Table I).

B. SWOT and KaRIN

The Surface Water and Ocean Topography (SWOT) mission will be implemented by National Aeronautics and Space Administration and Centre National d'Etudes Spatiales (CNES) in the coming decade. SWOT will provide 2-D topography information over the oceans and inland fresh-water bodies. [20] and [8] provide an updated description of SWOT's objectives, principle, and scientific requirements.

SWOT's main instrument is the Ka-band radar interferometer (KaRIN), a synthetic aperture radar interferometer with a ground swath about 120 km wide [Fig. 1(a)]. KaRIN will be complemented by a Jason-type nadir-looking altimeter among others (e.g., microwave radiometer to derive a wet troposphere correction, precise orbit determination (POD) payload, etc.)

References [22] and [8] explain how radar interferometry uses a measurement of the relative delay between the signals measured by two antennas separated by a known distance (baseline), together with the system ranging information, to determine surface elevations in a cross-track swath. The interferometric triangle [Fig. 1(b)] formed by the baseline B and the range distance to the two antennas r1 and r2 can be used to geolocate off-nadir points in the plane of the observation. The range difference between r1 and r2 is determined by the relative phase difference between the two signals as given by $\Phi = 2kr_1 - 2kr_2 \approx 2kB.\sin(\theta)$ where k is the electromagnetic wavenumber. From these measurements, the height h above a reference plane can be obtained [22] using the equation $h = H - r_1 \cos(\theta)$.

TABLE I
OVERVIEW OF CROSS-CALIBRATED ERROR CAUSES AND IMPACT ON TOPOGRAPHY

Cause	Amplitude of cause	Impact on topography (uncorrected)
Misconception on actual value of baseline roll angle	1 arcsec (i.e. 1°/60'/60" = 0.00028°)	Linear signature (35cm on outer swath edge)
Misconception on actual baseline length value	1 mm (i.e. 0.0001%)	Quadratic signature (40cm on outer swath edge)

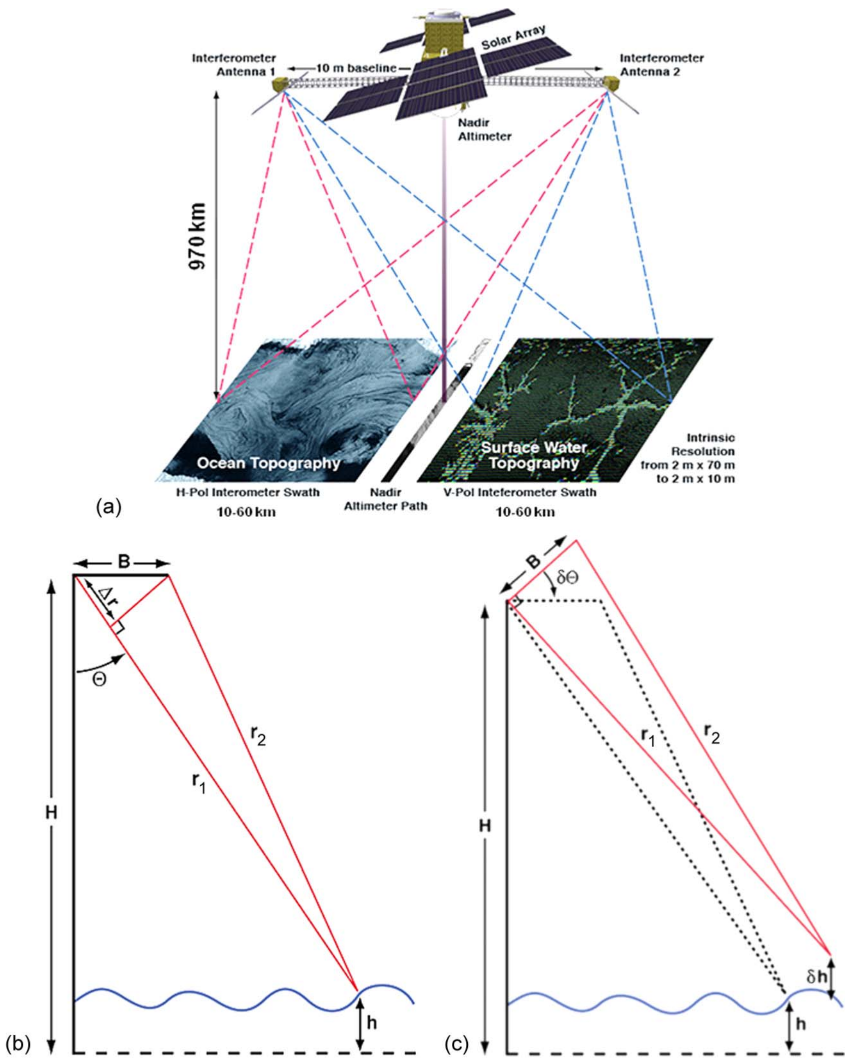

Fig. 1. Conceptual overview of KaRIN, (a) SWOT's Ka-band radar interferometer, (b) KaRIN's interferometric measurement concept, (c) and consequence of a non zero roll angle.

The orbit envisioned [20] for SWOT is circular and defined by 13 + 15/22 revolutions per day (i.e., an altitude of about 970 km) and an inclination of 78°. Consequently, it features a 22-day revisit time (i.e., repeat cycle), and each cycle is composed of about 300 revolutions or 600 tracks. At 0° N, the distance between neighbor tracks is approximately 130 km, allowing global coverage. The orbit also features 3-day westwards propagating subcycles similar to the subcycles of the TOPEX/Jason orbit. In other words, every 3 days, SWOT will provide a relatively homogeneous sampling at global scale. The 22-day sampling is then composed of interleaved 3-day subcycles. This configuration incidentally creates overlaps between neighbor swaths that increase with latitude (about 50% overlap for midlatitudes), that is to say duplicate measurements of the same location with 3-day difference. A different orbit is also envisioned for the CalVal and commissioning phase: it features a 3-day repeat cycle with about 1000 km between neighbor swaths (no overlap except at high latitudes).

SWOT has two main objectives [18]: to understand mesoscale and submesoscale processes, and to understand the water cycle over land. [11] and [8] highlight the stringent requirements in terms of error control. To be an order of magnitude below the signal, the error budget must be one decade below the signal spectrum, i.e., at centimetric level for 1-km resolution on ocean (i.e., more than five times more stringent than the accuracy observed on Jason-class pulse-limited altimeters). For hydrology, all lakes greater than 250×250 m^2 must be measured with a vertical precision of at least 10 cm and river slope must be measured to within 10 μrad (1 cm $\setminus$ km^{-1}).

C. Rationale of This Study

Because of the challenging requirements of SWOT, one of the most critical topics that will be addressed during the mission definition is the error allocation. In other words, what are all the sources of error, what fractions of the topography spectrum could be affected by each error source, and what will be used (hardware specification, processing, etc.) to ensure that the scientific requirements are met.

In this context, the purpose of this paper is to highlight the potential benefits of an error reduction processing that can be applied to SWOT's topographic data: an empirical cross-calibration of SWOT's geographically coherent errors using external references and the constellation of concurrent pulse-limited altimeters (e.g., Jason-CS or Sentinel-3C).

While this study should be carried out in the context of detailed error allocations of SWOT's data, the detailed analysis of the error allocation is extremely complex and beyond the scope of this paper. Consequently, and because we use Level-2 topography information as an input, our approach is to consider that SWOT's mission requirements [18], [8] are met on all errors but the ones that we try and reduce with empirical algorithms (see Section I-D).

The rationale is that the algorithms developed here could be used either as a risk reduction plan, or to improve SWOT's product beyond the original requirements. The algorithms presented in this paper are not needed at this stage of the mission definition. Moreover, the purpose of this paper is to go beyond simple error mitigation schemes (e.g., [9]) and to develop an empirical cross-calibration framework (defined in Section II) able to cope with larger input error levels, or more problematic topography spectrum contamination if left uncorrected (e.g., cross-track trends and curvatures that could be misinterpreted as actual topography features).

The framework presented in this paper exploits as much *a priori* statistical information as possible (error modeling, knowledge on dynamics and errors, topography first guess, reference field) to perform a quasi-optimal problem inversion. For the purpose of this demonstration, two SWOT error sources are considered: the so-called "baseline roll" error (or roll error) and the "baseline length" error. Yet, this process is basically applicable to any wide swath sensor as long as the error to be corrected is spatially and/or temporally coherent (more details given in Section II-A).

D. Error Sources Considered in This Paper

1) Baseline Roll Angle: The first error source considered in this paper is the "baseline roll" error. The interferometric equations show (e.g., [9]) that if the instrument is not oriented precisely in the Nadir direction see [Fig. 1(c)], the topography measurement h is corrupted by an error δh that is directly proportional to the sine of the roll angle. For KaRIN and very small angles, the roll error can be approximated by $\delta h = x.$ R, where R is the roll angle value and x the measurement position in the cross-track direction.

Assuming an outer edge position of 60 to 70 km and a very small pointing error of 1 arcseconds (i.e., about 0.00028° or 5 μrad) the roll topography signal is as large as 35 cm on the outer edges of the swath. Fortunately, since the error has a predetermined linear signature in the cross-track direction, it can be perfectly corrected if the true value of the roll angle is perfectly known. Consequently, the roll error is not an error due to the mispointing of the antennas, but an error stemming from an imperfect knowledge of their true roll angle.

The error made on the true roll angle of KaRIN's antennas can either be created by a nonperfect information about the attitude of the satellite itself (e.g., residual errors from gyroscope measurements), or from an angular deformation of the instrument mast (e.g., roll angle measured at the center of the baseline, not at the outer edges where the antennas are located). The baseline will be 2×5 m long [Fig. 1(a)], and assuming an extremely small mistake of 0.1 mm of the position of one antenna (outer edge of the mast), the apparent roll angle is 2 arcseconds, and the consequent topographic error is 70 cm. To be compatible with SWOT's centimetric requirements on topography, it is critical to know the exact position of each KaRIN antenna at all times.

Two residual roll signatures could be observed in practice: 1) at very low frequencies (e.g., satellite revolution) and 2) at high frequencies (a few Hz or more). The former could be generated by a nonperfect knowledge of the satellite (e.g., gyro error or slow thermal effects) or a flexible instrument baseline. The latter could appear if the baseline is very rigid and if a mechanical resonance of the mast is pushed (i.e., excited) by movements in the platform (e.g., maneuvers, solar panels, thermal snaps, etc.).

The actual extent of residual positioning errors of the antennas requires in-depth mechanical and thermal analyses of both the instrument (mast) and the platform. Yet, one can assume that baseline deformations and positioning errors will be minimized at instrument and satellite design level to be compatible with the scientific requirements. To that extent, the roll signal amplitude and frequencies simulated in this paper should be considered beyond the worst cases envisioned at this stage of the SWOT mission design.

Our purpose is to demonstrate the feasibility of empirical roll reduction techniques on Level 2 products (i.e., topography products for scientific users, as opposed to Level 0 or Level 1B data with instrumental, or technical parameters), assuming that all scientific requirements are met on SWOT's error budget except on the roll error.

2) Baseline Length: The second error source considered in this paper is the "baseline length" error. If the true distance between KaRIN's antennas is not the expected baseline length, the interferometric equations show (e.g., [9]) that an error appears on the topographic measurement. For KaRIN, the baseline length error can be approximated by $\delta h = (x^2.\delta B)/(B.H)$ where B is the expected baseline length, δB is the variations around this length, H is the altitude of the satellite, and x is the measurement position in the cross-track direction.

Like the roll error, the baseline length error can be perfectly corrected if the distance between KaRIN's antennas (baseline length) is perfectly known at all times. Thus, the actual error is stemming from an imperfect knowledge of the true baseline length. Possible causes of changes in the baseline length include mechanical perturbations (e.g., maneuver and platform pushing on the instrument mast) and thermal effects (e.g., slow thermal dilation and/or rapid thermal snaps).

For an altitude of about 970 km, an error of 0.1 mm on the knowledge of actual interferometric baseline length (10 m long) creates a cross-track quadratic signature approximately equal to 4 cm on the outer edges of the swath (60 to 70 km). Thus, it is important to know the exact distance between KaRIN's antennas at all times.

Like angular deformations, variations of the baseline length should be stringently limited at instrument design level (e.g., material used, deployment mechanism, etc.), or processing level (e.g., thermal models to correct from snaps in and out of eclipse phases). To that extent, the amplitude and frequencies we use to simulate an imperfect knowledge of the true baseline length should be beyond the worst cases expected for SWOT.

Our purpose is to demonstrate the feasibility of empirical error reduction techniques on Level 2 topography products, assuming that all scientific requirements are met on SWOT's error budget except on the baseline length error.

II. Empirical Cross-Calibration: Overview

This section outlines the techniques used in this paper to locally estimate the baseline roll and length errors over cross-calibrations zones (Section II-A and Section II-B), as well as the end-to-end approach used to provide a global multisurface correction at all times (Section II-C).

A. Empirical Cross-Calibration: General Principle

The principle presented in this paper can be used if some premises are met. The errors must have a spatially and/or temporally coherent signature on the measured variable (here topography). The signature must be modeled. Even random or unpredictable errors can be corrected if an analytical model can describe their signature, or correlation in space or in time, or the link with other measured parameters. For instance, this technique can reduce SWOT's roll error (spatially coherent due to the cross-track linearity) or the orbit error (due to the temporal correlation) but not random noise. Furthermore, the errors must be spectrally separable from the signal of interest (e.g., if wet troposphere errors overlap the oceanic topography spectrum, they cannot be corrected empirically) or the signal of interest will be absorbed and corrupted by the empirical correction.

Starting from the true topography $H_{\rm real}$ measured by SWOT, we assume that SWOT gives $H_{\rm obs}$, the sum of $H_{\rm real}$ plus various error terms. Then, we assume that some of these errors cannot be minimized (e.g., noise). The uncorrected errors are lumped together as ε, which is a function of the measurement's position and time.

Conversely, we assume that some error terms can be cross-calibrated, and we define a model to describe them. Because the errors are decomposed as cross-track and along-track components, our model uses functions of time t (i.e., the position in the along-track direction) and x (position of the measurement in the cross-track direction). The roll error is created by the true roll angle R of the KaRIN antennas. This roll is a function of time so we use R(t). The topographic error created has a linear across-track signature (see Section II-D1) so its model is the product of x and R(t). Similarly, the signature of the baseline length error is a function of $\delta B(t)$, the baseline length variations as a function of time. The error signature is quadratic in the cross-track direction and defined as the product of x^2 and $\delta B(t)$ divided by the satellite altitude a and the nominal baseline length B.

Therefore, in a simplified model, SWOT's measurement is decomposed as the sum of the true topography signal, plus coherent error signatures, plus the sum of all other errors:

$$\mathbf{H_{obs}(x,t) = H_{real}(x,t) + x.R(t) + x^2/a.\boldsymbol{\delta} B(t)/B + \boldsymbol{\varepsilon}(x,t)}. \quad (1)$$

From (1), one can see that it is possible to extract R(t) and $\delta B(t)$ empirically using measurements $H_{\rm obs}$ (x,t) as the dependent variable and x as the explanatory variable. In turn, these estimates of R and δB can be used to correct $H_{\rm obs}$ from the coherent signatures.

Although it is technically possible to perform simple linear or quadratic fits on $H_{\rm obs}$ in the cross-track direction at each time step and everywhere to get R and δB, this is a poor idea for SWOT because the premise of spectral separation is not met: the empirical fit would be absorbing a fraction of $H_{\rm real}$ as well. Consequently, actual topography gradients and curvatures in the across-track direction would be misinterpreted as R and δB and "empirically removed" from SWOT's images. To that extent, all cross-calibration algorithms consider that ε, but also $H_{\rm real}$ are perturbations of their objective (here measuring R and δB). Therefore, the main difficulty in the empirical approach is to mitigate coherent errors while not absorbing $H_{\rm real}$.

B. Experience of Pulse-Limited Altimetry: Similarities and Differences

The techniques detailed in Sections III and IV are largely derived from operational processing applied in traditional pulse-limited altimetry (e.g., [7]). One classical need of altimetry users is to remove POD errors. Although POD solutions are very good for recent missions, and notably for the TOPEX/Jason series, less precise altimetry satellites (e.g., ERS or GFO) must be cross-calibrated to remove regional biases of their 1-D topography profiles. Because POD error is geographically coherent and dominated by one and two cycles per revolutions signals (thousands of kilometers), it is possible to use the empirical approach from Section II-A (with a POD error model instead of a baseline roll/length error model).

Reference [24] uses sinusoidal models, while [13] uses splines instead. In both approaches, ε and $H_{\rm real}$ are sources of perturbations of the POD error estimates. To minimize this influence, both groups use cross-over points as an input observation. Indeed, when two altimeter profiles are crossing over, there is one common measurement location to both satellite tracks. If the temporal distance between the measurements from each profile is short enough, a large fraction of ε and $H_{\rm real}$ cancel out in the difference between the topography from each profile.

In a different context, Labroue *et al.* [25] has performed a sea state bias error reduction using the empirical approach (using a nonparametric model as a function of retracked significant wave height and sigma0 or wind speed modulus). Labroue *et al.* notably used different techniques (namely crossover, collinear, and direct) to minimize the absorption of ε and H_{real} in their empirical sea state bias solutions, and they highlight differences between these methods.

The following sections make an extensive use of pulse-limited altimetry cross-calibration, but the problem tackled with SWOT's errors is significantly different. In pulse-limited altimetry, inversions are performed globally. For instance a 2-month to 1-year database of cross-over point differences is used to perform a global minimization using the empirical models. For SWOT, a global minimization is not possible due to the amount of data (2-D images instead of 1-D profiles, and kilometric resolution). Hence, we use a two-step approach instead.

We inverse (1) (i.e., we obtain R and δB estimates from H_{obs} measurements) on small scenes, a.k.a cross-calibration zones. Because cross-calibration zones can overlap (or be separated by transition zones such as coastal zones), we use an optimal along-track propagation mechanism (1-D objective analysis) to derive a correction at all times: in cross-calibration zones, in overlaps, and in transition zones.

C. Application to SWOT's Coherent Errors

The first step of the SWOT empirical cross-calibration process is to perform the local inversions of Equation 1 over so-called cross-calibration zones. Like for pulse-limited altimetry, we use two techniques to minimize the influence of ε and H_{real} on the estimation of R and δB.

1) The direct method takes SWOT scenes (t_0 and t_1 are the temporal/along-track boundaries), and it uses a first guess H_{ref} to account for the bulk of H_{real} (e.g., digital elevation model (DEM) on land, or low-resolution sea surface height map on ocean). Removing the first guess H_{ref} also removes a large fraction of the spectral overlap between the topography signal of interest and the error signatures. Consequently, it is possible to empirically adjust R(t) and $\delta B(t)$ on the difference between H_{obs} and H_{ref}, because a strong premise of empirical cross-calibration method (spectral separation) is now met. The direct method is detailed in Section III-A.
2) The cross-over method uses overlaps between two arcs of satellite data, one ascending, and one descending (Figs. 2 and 3). Near the cross-over point of both arcs, it is possible to find two datasets which can be geographically colocated. Consequently, we obtain two values of H_{obs} on a single location. The temporal distance between both samples (t and t') can be as short as a few hours, or as long as a full SWOT cycle. If we limit the observation to crossovers with a relatively short temporal distance between the ascending and the descending arcs, it is possible to make the approximation that a large fraction of ε and H_{real} is cancelled out in the cross-over difference $H_{\text{obs}}(t') - H_{\text{obs}}(t)$. Spectral separation with error signatures is incidentally achieved and R(t) and $\delta B(t)$ as well as $R(t')$ and $\delta B(t')$ can be estimated as an adjustment on the cross-over topography differences. The cross-over method is detailed in Section III-B.

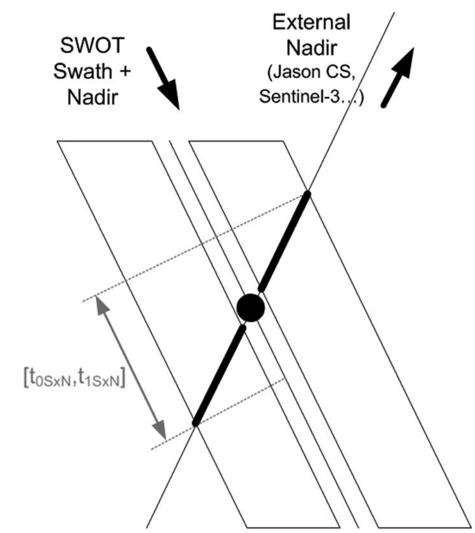

Fig. 2. Geometry of the cross-calibration segments between KaRIN and concurrent Nadir altimeters. The black circle is the Nadir/Nadir cross-over point, the black segments are highlighting the overlap between the SWOT swath and the Nadir track. In these segments, only SWOT interferometric measurements must be cross-calibrated, and the Nadir data set provides an uncorrupted topography reference. The gray arrow shows the along-track segment where the whole swath can benefit from a cross-calibration performed on the black segments.

In this paper, we implement the direct method and the cross-over method, both on land and on ocean. We derive local roll and/or baseline length estimates from inversions performed on cross-calibration zones: SWOT scenes and cross-over diamonds.

Although local inversions from Section III theoretically provide nearly a global coverage, some areas are difficult to process for various reasons (e.g., due to the presence of rapid coastal features or strong mesoscale features which are not completely removed before the inversion). Conversely, two different inversion techniques can sometimes be used to provide overlapping local roll estimates on the same SWOT image.

The geometry and the geographical distribution of cross-calibration zones are method specific (discussed in Section VI). Moreover, each technique has intrinsic local errors (e.g., corruption by Digital Elevation Model (DEM)) errors is regional specific), and the sensitivity to the transition between land and ocean (resolution, dynamics, error sources) is again method specific (discussed in Sections V and VI).

Merging the contribution of all estimates from all surfaces and methods is therefore needed to compute a coherent and global correction at each time step (in and out of cross-calibration ones): to fill the gaps, and to find the truth between estimates in disagreement. We use a 1-D objective analysis (or optimal interpolation or O.I) to perform the propagation. The end-to-end scheme is therefore a two-step process shown by Fig. 4: first, we compute local estimates (Section III), and second, we compute the global correction (Section IV).

III. LOCAL ESTIMATES

This section gives more details about the local cross-calibration estimates obtained with the direct method (Section III-A) and with the cross-over method (Section III-B).

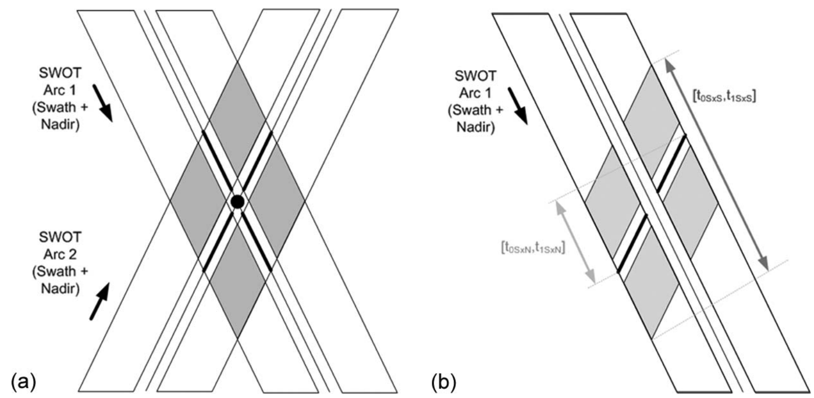

Fig. 3. Geometry of the cross-calibration zones between two SWOT arcs (a). Gray areas contain overlapping measurements from the interferometric data sets, black segments are overlaps between the Karin and the onboard Nadir (i.e., traditional) altimeter, and the black circle is the Nadir x Nadir cross-over point. Each crossover gives two along-track segments (gray arrows in subplot b): one is associated with Karin x Nadir overlaps (light gray), and the other to Karin x Karin overlaps.

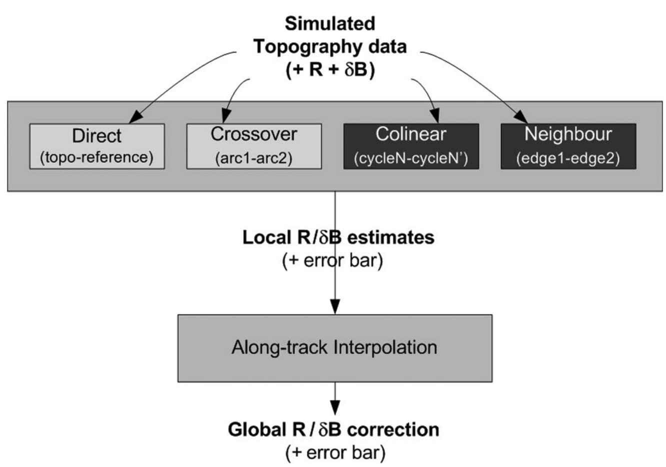

Fig. 4. Overview of SWOT's empirical cross-calibration scheme.

From these methods, it is also possible to derive other cross-calibration techniques (discussed in Section VI-E).

A. Direct Method

The direct method uses H_{ref}, an external information (e.g., model output, reference surface) to account for the bulk of the true topography variations H_{real} in the measurement H_{obs}. If we use the difference Y between H_{obs} and H_{ref}, we replace H_{real} from (1) (total signal), by $\delta H(x,t)$ from (2), that is to say only short scale and/or rapid components of H_{real} that were not in the first guess H_{ref}.

$$\begin{aligned}\mathbf{Y}(\mathbf{x},\mathbf{t}) &= \mathbf{H_{obs}}(\mathbf{x},\mathbf{t})-\mathbf{H_{ref}}(\mathbf{x},\mathbf{t})\\ &= \mathbf{x}.\mathbf{R}(\mathbf{t})+\mathbf{x^2}/\mathbf{H}.\boldsymbol{\delta}\mathbf{B}(\mathbf{t})/\mathbf{B}+\boldsymbol{\delta}\mathbf{H}(\mathbf{x},\mathbf{t})+\boldsymbol{\varepsilon}(\mathbf{x},\mathbf{t}). \quad (2)\end{aligned}$$

As highlighted in Section II-C, the proxy H_{ref} is used to meet the premise of spectral separation, thus allowing the error signatures to be adjusted on residuals. The problem is then simple and linear: the observations Y are located in each pixel of the SWOT swath, and the parameters to be obtained are R(t) and $\delta B(t)$.

Each scene is processed with an optimal inverse method described by [5]:

$$\mathbf{R_{est}} = \mathbf{C_{xx}}.\mathbf{M^T}.(\mathbf{M}.\mathbf{C_{xx}}.\mathbf{M^T}+\mathbf{C_{vv}})^{-1}\mathbf{Y} \qquad (3)$$

where R_{est} is the estimated vector of R(t) and/or $\delta B(t)$, M is the observation model mapping the state space to the observed space (e.g., linear or quadratic signature models), and Y the topography measured by SWOT and corrected from the *a priori* first guess or reference [(2)].

R and δB can be estimated at each time step in the cross-calibration scene. This is unnecessary if we assume that they contain only low-frequency signal, but there are two advantages to this method: 1) to cope with high-frequency errors if necessary, and 2) the along-track spectrum is better controlled with an optimal inverse method which requires these degrees of freedom. To that extent, the inversion is optimally constrained by *a priori* statistical knowledge on the signal or on the observation error, that is to say by known statistical characteristics of R, δB, δH, and ε.

The matrix C_{xx} contains the covariance of the observation states, i.e., the along-track normal modes, correlations, or amplitudes. In other words, this matrix contains the expected variance and correlation of R and δB (e.g., derived from thermal or mechanical analyses of the platform and of instrument mast). In this matrix is also defined possible correlations between two variables (for instance if R and δB are expected to be linked).

The matrix C_{vv} is the observation error covariance. Any information on the amplitude, frequencies, geographical variations, or temporal coherency of the error affecting Y is put into C_{vv}. As an illustration, if the DEM used for H_{ref} is known to contain uncorrelated errors, then there is a known error on Y, and this error is put in the C_{vv} error budget (as noise on the variance diagonal, possibly with geographical variations).

Similar setups are used for known correlated error terms of δH and ε. Because nonzero residuals of $H_{\mathrm{real}} - H_{\mathrm{ref}}$ are corrupting Y (the observation used to estimate R and δB), an approximation of this error is put in C_{vv} including variance, decorrelation scales, or space and time variations. References, [15] and [16] estimated the differences between H_{ref} and H_{real} on ocean by measuring the limitations of pulse-limited altimetry satellites to reconstruct a proxy (H_{ref}) of the sea surface height fields using eddy resolving models (H_{real}). This difference was shown to be correlated but also geographically and temporally coherent.

One of the advantages of the optimal inverse method from [5] is that it provides not only better results but also a good error covariance of the estimated parameters. Contrary to some inversion techniques (and notably simple least square methods), the error covariance matrix is trustworthy if the *a priori* knowledge set into C_{xx} and C_{vv} is realistic. The error covariance E_{xx} is given by:

$$\mathbf{E_{xx}} = \mathbf{C_{xx}} - \mathbf{C_{xx}}.\mathbf{M^T}.(\mathbf{M}.\mathbf{C_{xx}}\mathbf{M^T} + \mathbf{C_{vv}})^{-1}.\mathbf{M}.\mathbf{C_{xx}}. \tag{4}$$

To validate the input error setup in C_{xx} and C_{vv}, we also perform the inversion with simple least squares like [9], that is to say with absolutely no statistical knowledge of the problem to be solved. The inversion equations are then much simpler

$$\mathbf{R_{est}} = (\mathbf{M^T}.\mathbf{M})^{-1}.\mathbf{M^T}.\mathbf{Y} \tag{5}$$

$$\mathbf{C_{xx}} = (\mathbf{M^T}.\mathbf{M})^{-1}. \tag{6}$$

The size of the inversion (or linear problem solved) with simple least squares is N.N where N is the number of state variables (i.e., number of time steps where the R and δB are estimated, or even fewer parameters if each signal is approximated by polynomial functions), while the size of the matrix for an optimal inverse method is $N' \times N'$ where N' is the number of input observations (i.e., all SWOT pixels in the scene). In other words, the optimal method is exceedingly more computationally intensive, particularly on land with SWOT's high-resolution products. To that extent, the experiments presented in Section V use preprocessed input observations with a lower resolution, and nonoverlapping and size-limited along-track scenes. In practice, the cross-calibration algorithms are less demanding than other SWOT ground processing steps, and by SWOT's launch date, the inversion could be done on larger scenes at higher resolution, particularly once the implementation is numerically optimized.

B. Cross-over Method

The cross-over method is using two types of crossovers: overlaps between KaRIN swaths and pulse-limited nadir tracks (either from SWOT's Jason-class instrument, or from concurrent topography missions), and overlaps between different KaRIN swaths. They are presented in Sections III-B1 and III-B2, respectively.

1) Nadir/KaRIN Cross-over Segments: Fig. 2 shows the geometry of a Nadir x SWOT crossover. When a SWOT swath crosses the track of a pulse-limited altimetry satellite (e.g., tentatively Jason-CS, or Sentinel-3C), two KaRIN x Nadir cross-calibration segments are created, one from the left 1/2 swath, and one from the right 1/2 swath (black lines in Fig. 2).

Contrary to KaRIN data, the nadir-derived topography H_{nadir} is not affected by the baseline roll or baseline length errors. It is therefore possible to use it to minimize the impact H_{real} and ε in the inversion, like with H_{ref} in the direct method. However, there is an underlying approximation that H_{real} and ε are stationary between the measurement times t and t' of each sensor. Consequently, the temporal distance between both colocated measurements must be short enough to cancel out H_{real} and ε in the cross-over difference, and it is not possible to use every possible cross-over location. An additional constraint is used to keep only crossovers with a short temporal difference between the ascending and descending arcs. Like [13], we have used 10 days as the temporal limit to cancel out a large fraction of mesoscale topography signals on ocean. Equation (2) thus becomes

$$\begin{aligned}\mathbf{Y}(\mathbf{x},\mathbf{t},\mathbf{t'}) &= \mathbf{H_{obs}}(\mathbf{x},\mathbf{t}) - \mathbf{H_{nadir}}(\mathbf{x},\mathbf{t'}) \\ &= \mathbf{x}.\mathbf{R}(\mathbf{t}) + \mathbf{x^2}/\mathbf{H}.\boldsymbol{\delta}\mathbf{B}(\mathbf{t})/\mathbf{B} + \boldsymbol{\delta}\mathbf{H_{hf}}(\mathbf{x},\mathbf{t'}-\mathbf{t}) \\ &\quad + \boldsymbol{\delta\varepsilon}_{\mathbf{hf}}(\mathbf{x},\mathbf{t'}-\mathbf{t})\end{aligned} \tag{7}$$

where δH_{hf} and $\delta\varepsilon_{\mathrm{hf}}$ are the rapid fractions H_{real} and ε that do not cancel out in the cross-over difference. The inversion is performed on each Nadir x KaRIN crossover, thus providing a small along-track segment $[t_0, t_1]$ where R and δB are estimated (gray arrow in Fig. 2).

The problem is solved with the same optimal inversion as in Section III-A. The configuration of C_{vv} is slightly different because the modeling of δH_{hf} and $\delta\varepsilon_{\mathrm{hf}}$ can be different from the modeling of δH and ε. For instance, in the direct method, residual oceanic variability (i.e., the information not already provided by H_{ref}) is systematically accounted for in C_{vv}, whereas it is not necessarily the case for crossovers if the delta time $t - t'$ is very small. For the latter, only the shortest scales and most rapid signals need to be modeled in C_{vv}.

2) KaRIN/KaRIN Cross-over Diamonds: Fig. 3 shows the geometry of SWOT x SWOT crossovers. The cross-over zone is a large diamond composed of four small diamonds (overlaps between the left and right 1/2 KaRIN swaths from each arc), and four segments (overlaps between the pulse-limited nadir track from one arc, and the two 1/2 KaRIN swaths from the other arc), and one cross-over point (intersection between the nadir tracks).

In the small gray diamonds from Fig. 3(a), it is possible to precisely colocate two measurements from KaRIN. If the delta time between the arcs is sufficiently small, each measurement is observing a common value of H_{real}, and to some extent of ε. Conversely, measurements are affected by two different values of R and δB topography signatures. First, because R(t) and $\delta B(t)$ have changed between the measurement time t of the first arc and the measurement time t' of the second arc. Second, because the relative cross-track distances to their respective nadir track [x in (1)] are different even if the data are on common longitude/latitude points. The observation Y then becomes

$$\begin{aligned}\mathbf{Y}(\mathbf{lon},\mathbf{lat},\mathbf{t}) &= \mathbf{H_{obs}}(\mathbf{lon},\mathbf{lat},\mathbf{t}) - \mathbf{H'_{obs}}(\mathbf{lon},\mathbf{lat},\mathbf{t'}) \\ &= \mathbf{x}.\mathbf{R}(\mathbf{t}) + \mathbf{x^2}/\mathbf{H}.\boldsymbol{\delta}\mathbf{B}(\mathbf{t})/\mathbf{B} - \mathbf{x'}.\mathbf{R}(\mathbf{t'}) \\ &\quad - \mathbf{x'^2}/\mathbf{H}.\boldsymbol{\delta}\mathbf{B}(\mathbf{t'})/\mathbf{B} + \boldsymbol{\delta}\mathbf{H_{hf}}(\mathbf{lon},\mathbf{lat},\mathbf{t'}-\mathbf{t}) \\ &\quad + \boldsymbol{\delta\varepsilon}_{\mathbf{hf}}(\mathbf{lon},\mathbf{lat},\mathbf{t'}-\mathbf{t}).\end{aligned} \tag{8}$$

Thus, in place of a direct measurement of the baseline roll and baseline length signatures in Y, the cross-over diamonds give an observation of the difference between the signature of R(t) and $\delta B(t)$ on the first swath, and $R(t')$ and $\delta B(t')$ on the second swath. Like in Nadir x KaRIN crossovers, the cross-calibration input Y is potentially altered by rapid topography changes δH_{hf} or rapid error changes $\delta\varepsilon_{\mathrm{hf}}$.

Fig. 5 shows the ribbon-shaped topography error created by the linear signature at each time step (top) of the baseline roll angle (bottom). The right-hand side plate of Fig. 5 also shows

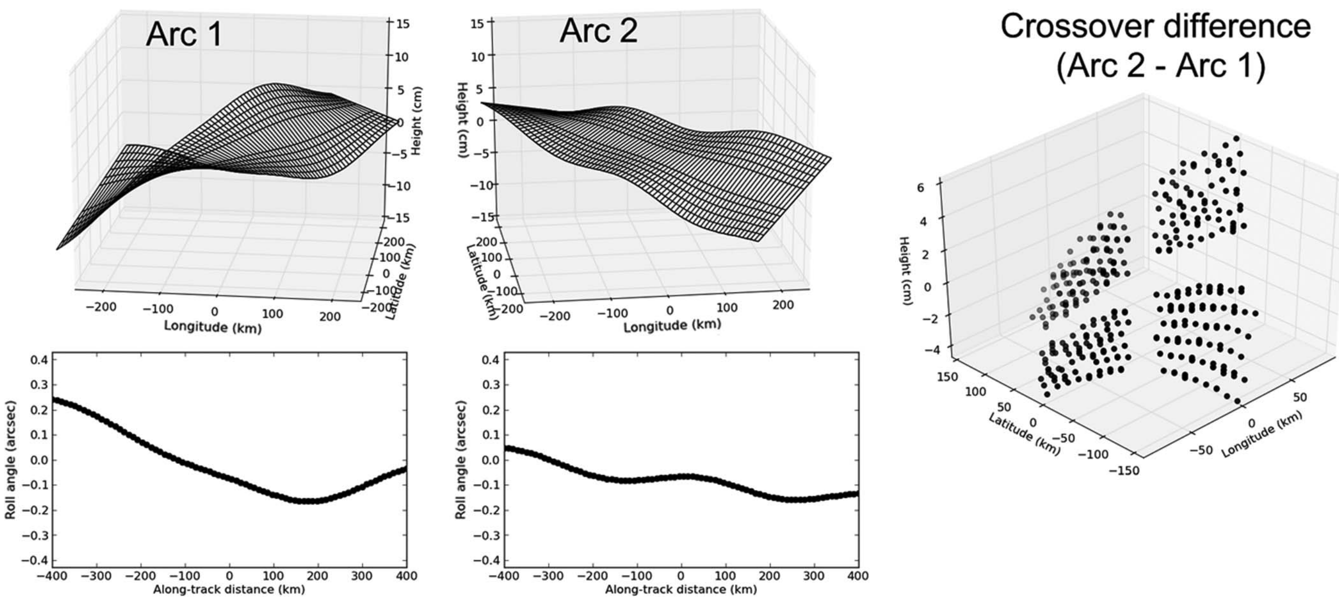

Fig. 5. Conceptual impact of the roll angle (bottom) on the KaRIN's topography (top) for two crossing swaths (left and middle), and residual topography difference visible on cross-over observations (right). In this example, the difference of the two roll signatures exhibits a 100-km gradient (amplitude of 10 cm). Decorrelation scale used: 500 km (i.e., 70s).

the KaRIN x KaRIN cross-over topography differences. In this case, the cross-over difference primarily exhibits a gradient of about 10 cm over 200 km. The objective of the cross-over inversion method is to extract the ribbon-shaped roll signal of each arc from any other cause capable of creating such a gradient.

Fig. 6 shows the quadratic topography signature on the two 1/2 swaths (top) created by the baseline length errors (bottom), and the associated cross-over topography differences (right). In this example, the difference of the two signatures exhibits a coherent bell-shaped structure of 200 km by 300 km with an amplitude of 5 cm. Like for the roll error, the purpose of the estimation method is to extract actual error information from any other cause capable of creating such a coherent structure.

The problem from (8) can be solved with the same approach as in the direct method, although the matrices used are slightly different: the matrix M notably describes that Y is composed of the difference of two coherent signatures, and C_{xx} describes potential correlations between the two arcs if the temporal distance between t and t' is short enough. Similarly, C_{vv} must be tuned to account for high-frequency content δH_{hf} and $\delta\varepsilon_{\mathrm{hf}}$ only.

The positions of SWOT's measured pixels H_{obs} may not be exactly the same in both arcs. From a practical point of view, it is very important to perform a precise reregistration in space and time so that the longitude, latitude, t, and t', x and x' are perfect matches. This is done either with pre-interpolation before the problem is solved or (better) during the inversion itself through the matrix M: the observation model mapping the state space (R and δB) to the observed space (topography) is no longer limited to linear or quadratic signatures; it also features the temporal/along-track coregistration.

Lastly, because we assume that there is a Jason-class nadir capability on SWOT, the Nadir/KaRIN segments from Fig. 3(a) give additional inputs for the inversion. In practice, we perform a concurrent inversion of both arcs using all the overlapping data (KaRIN/KaRIN and KaRIN/Nadir). We simultaneously estimate the value of R(t) on $\delta B(t)$ on each arc, along both cross-calibration segments [gray arrows in Fig. 3(b)].

IV. Global Correction

The inversions from Section III give local estimates of R and δB, derived from one or multiple methods, obtained on one or multiple surfaces (land, ocean), exploiting SWOT only or concurrent altimeters as well. The many local estimates then need to be complemented by an along-track propagation mechanism to provide a global correction at each time step (see Section II-C).

Here, we assume that the baseline roll error and the baseline length error are not correlated. We can then perform individual interpolations as we do not need to exploit the covariance between both variables. Each cross-calibration zone provides a block $[t_0, t_1]$ of local inputs $R_{\mathrm{obs}}(t)$ defined by

$$\mathbf{R_{obs}(t)} = \mathbf{R_{real}(t)} + \mathbf{e(t)} \tag{9}$$

where R_{real} is the actual value of the signal to be interpolated and e the estimation error of the local cross-calibration from Section III. The input of the interpolation method is both the local estimate of R_{obs} (or δB_{obs}) plus a theoretical knowledge (estimated covariance) of its error. Indeed, the formal or theoretical error given by (4) is trustworthy if the problem is well described (shown in Section V).

The interpolation can be done with simple methods without any *a priori* knowledge, such as with spline interpolators [9] or kernel smoothers, or with very constrained models (e.g., harmonic functions) based on strong assumptions on the normal modes of the baseline distortion. When the signal to be corrected is very low frequency, the results obtained are equivalent.

However, the best interpolation scheme is obtained with optimal inverse methods, particularly when *a priori* statistical knowledge about the problem can be exploited (e.g., correlation

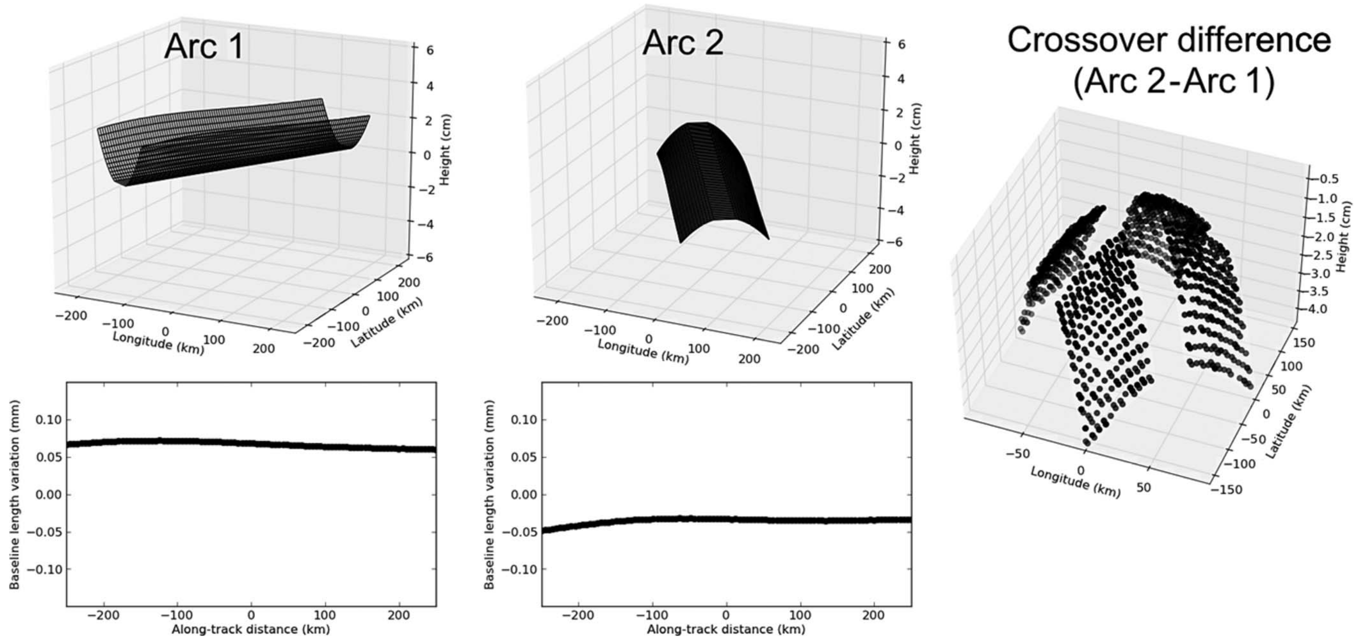

Fig. 6. Conceptual impact of the baseline length variations (bottom) on the KaRIN's topography (top) of two crossing swaths (left and middle), and residual topography difference visible on cross-over observations (right). In this example, the difference of the two baseline length signatures exhibits a coherent bell-shaped structure of 200 km by 300 km (amplitude of 5 cm). Decorrelation scale used: 500 km (i.e., 70s).

distance), and when the signal includes a significant fraction of relatively short wavelength signals (e.g., ranging from 7 to 150 s i.e., 50 km to 1000 km along track) or nonstationary signals. Moreover, if we assume that baseline roll and baseline length are affected by thermal snaps (i.e., offsets when the satellite goes in and out of eclipse), the objective analysis can be configured to process each segment independently (from offset to offset). In our simulations, the interpolation is done with a 1-D objective analysis ([5]):

$$\mathbf{R_{int}} = \mathbf{C_{xx}}.\mathbf{N^T}.(\mathbf{N}.\mathbf{C_{xx}}.\mathbf{N^T} + \mathbf{C_{rr}})^{-1}.\mathbf{R_{obs}} \qquad (10)$$

where R_{int} is the interpolated roll or baseline vector (one scalar at each time step), C_{xx} is the *a priori* knowledge of the normal modes, i.e., typical scales and variance statistically expected on R(t), C_{rr} is the input error covariance matrix (based on the output of the local inversion method, i.e., from the formal error covariance in cross-calibration zones), and N is the observation model mapping the state space to the observed space (e.g., the mapping between roll differences and two separate roll estimates).

The error description in C_{rr} is not limited to a standard deviation or noise level: if the error committed by a specific local estimation is a possible scene-specific bias, then the formal covariance error Exx from (4) does contain the correlation information. In other words, the observation R_{obs} is given to the interpolation with insights about potential correlated errors. This is done automatically through the inverse method error covariance, and no manual tuning is necessary.

V. End-to-End Simulation Results

A. Introduction

Many simulations have been carried out to validate the inversion and interpolation algorithms. Starting from ideal inputs (error free), more realistic simulations, and various sensitivity tests have been performed with degraded configurations (erroneous description of the signal/error in the matrices C_{xx}, C_{vv}, and C_{rr}). This section gives an overview of the end-to-end results (local estimation and global interpolation) in a typical case, and Section VI addresses some specific topics and notably the sensitivity to wrong inputs and configuration.

B. Basic Parameters

In all our simulations, we assume that a Jason-class nadir instrument is available on SWOT, but not the near-nadir processing mode of KaRIN (filling 2 × 10 km gap in the middle of the swath). We also assume that two concurrent altimeters are available for SWOT cross-calibration: one flying along the historical TOPEX/Poseidon track, and one along the Sentinel-3 track.

We use two components for H_{real}: one on land and one on ocean. On ocean, H_{real} is simulated using global model outputs (Mercator-Océan 1/12°, eddy resolving), and on land, we use a Shuttle Radar Topography Mission (SRTM)-derived DEM, and typical dynamics observed in fresh water databases (e.g., Hydroweb from LEGOS, 2011). Various error sources are added to obtain H_{obs} (see Table II): instrument noise, DEM imperfections, orbit error, wet troposphere errors, etc. Moreover, layover effects (i.e., the geometric distortion in radar images when the slope of the terrain is higher than the incidence angle) are approximated in a very simple way: taking the cross-track gradient of the DEM (relatively low resolution versus SWOT products), we apply an arbitrary screening if the cross-track gradient is larger than a threshold. We edit out about 25% of the data on land, often in a geographically coherent way.

Similarly, we use two components for the first guess H_{ref} of the direct method. On ocean, the proxy H_{ref} is constructed from pulse-limited altimetry: the first guess H_{ref} is simulated

TABLE II
ROLL SIMULATION INPUTS

Error	std	along track correlation	cross track correlation
Orbit error	2 cm	>5000 km	constant
Instrument (thermal noise) (Pixel 20 m x 90 m)	50 cm on water 3 m on land	random random	random random
Wet Tropo (optimistic & random)	5 cm	50 km	50 km
DEM (long wavelength)	2 m	>5000 km	>5000 km
DEM (short wavelength)	3 m	100 to 400 m	100 to 400 m

by interpolating H_{real} along the altimetry tracks of three arbitrary altimetry orbits (e.g., Jason-CS, Sentinel-3C, and SWOT's Jason-class instrument), adding realistic measurement errors from and reconstructing three-satellite sea surface topography maps from the simulated measurements. The resulting multi-nadir maps are similar to DUACS/AVISO products documented in [2] or [7]. The reconstructed H_{ref} fields thus implicitly include the limitations of low-resolution topography maps with respect to H_{real} (e.g., described by [16]). On land, we simulate H_{ref} by using H_{real} (SRTM-derived DEM) and adding a long wavelength error and a high-frequency error that are consistent with observations from [17] and [4].

C. Baseline Roll

The uncorrected roll angle signal simulated as an input is limited to relatively long wavelengths (no high-frequency vibration). Two test scenarios are considered (none of which should be considered as truthful of the SWOT error budget as per Section I-C):

- a simple scenario with an along-track correlation of 1 h or more (one or two cycles per revolution) with a roll signal amplitude of 0.3 arcseconds, i.e., up to 10 cm on the outer edges of the swath;
- a worst case roll scenario with a more rapid signal (correlated over 120 s or 800 km) and with a very large amplitude of 2 arcseconds, i.e., up to 70 cm on the outer edges of the swath.

An example of the ribbon-shaped signal induced by the roll angle is shown in Fig. 5. This signal is added to H_{real} and other errors. Then, the direct and cross-over methods are applied independently (Fig. 4) to derive local rol estimates. Fig. 7 shows the inversion outputs on a cross-over scene (ocean). Subplot (a) shows, as a function of latitude, the along-track value of the simulated roll signal in arcs (black) and the estimated value (red). The input roll contains relatively short-wavelength variations (700 km). The estimated values are consistent with the true roll angle albeit less accurate on the edges of the cross-calibration zone.

Subplot (b) shows the actual error (i.e., absolute value of the simulated roll minus the estimated roll) in red and the formal error (i.e., error predicted by the optimal inversion) in black. In this example, the average error on the entire scene is 0.03 arcseconds ($\sim$1 cm on topography). If the formal error is used to screen untrustworthy values, the average error on this scene is less than 0.02 arcseconds (subcentimetric). For partial crossovers (coast, missing data, etc.) or different cross-over geometries (different latitudes), the error can be significantly larger.

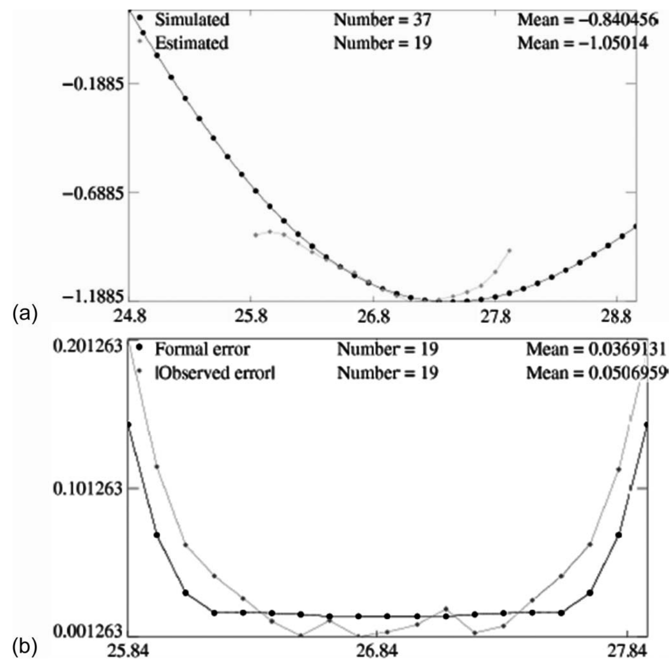

Fig. 7. Illustration of a cross-over scene inversion. Subplot a shows, as a function of latitude, the along-track value of the simulated roll signal in arcs (black) and the estimated signal (gray) on an arbitrary crossover. Subplot b shows the observed error (i.e., absolute value of simulated—estimated) in gray and the formal error (i.e., the error predicted by optimal inversion) in black.

Table III gives an overview of the average results obtained with the direct and cross-over methods on each surface. The low-frequency roll error (1 h or more) is well observed by all methods and slightly better on land crossovers because the topography is static out of fresh water bodies, whereas oceanic variability can be absorbed on ocean. The error is about 0.1 arcseconds for the simple problem (low-frequency roll).

In our worst case roll scenario, the cross-over method is less efficient on land. Indeed, land crossovers yield an average error of 0.4 arcseconds, whereas other methods give about 0.15 arcseconds. On land, the cross-over problem is more difficult to solve: layover effects are creating geographically coherent data gaps and therefore incomplete crossovers and observability issues (explained in Section VI-D).

The difference between the cross-over performance for both roll scenarios can be explained by the C_{xx} matrix of (3): in the low-frequency scenario, the empirical method smoothes over

TABLE III
SYNTHESIS OF THE AVERAGE RESULTS OBTAINED ON LOCAL ROLL ESTIMATION

RMS of simulated roll minus estimated roll (arcsec)	Ocean Crossover SW*SW	Ocean Crossover SW*J3	Ocean Crossover SW*S3	Land Direct (150km blocks)	Ocean Direct (assumed from MSS error)	Land Crossover SW*SW(crude layover simulation)
Low frequency roll	0.09	0.11	0.12	x	0.2	0.02
Worst case scenario	0.17	0.14	0.15	0.15	x	0.4

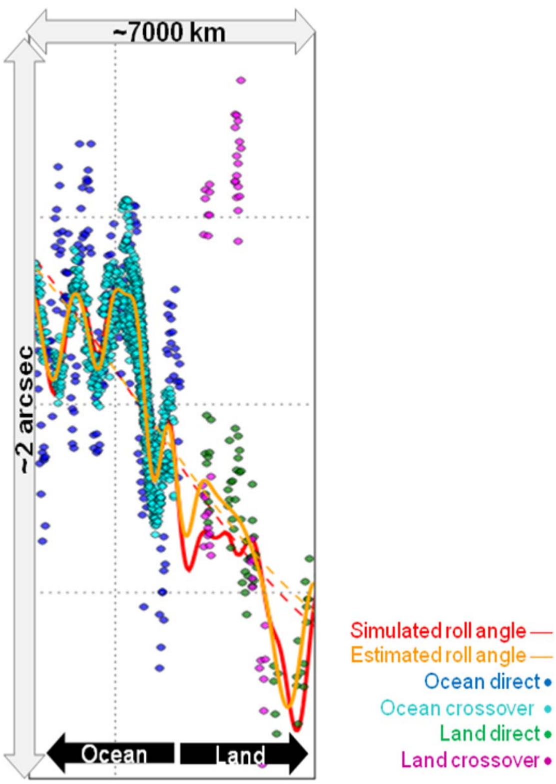

Fig. 8. Final along-track restitution on a transition between land and sea. The red curve shows the simulated roll signal (pessimistic scenario, with moderately high-frequency modes) to be estimated. The orange curve is the estimate given by the optimal interpolation. The blue, cyan, green, and pink dot colors correspond to different types of local inversions (inputs of the interpolation).

such observability errors because C_{xx} constrains the correlation of the estimated roll values, whereas the scales involved in the worst case scenario (800 km) force the inversion to absorb any observability error (signal/error not spectrally separable).

To summarize, local inversions can reduce the roll signal by a factor of 3 to 12. The residual topography error from such raw local estimates would be 3 to 5 cm on the outer edges of the swath. At this point all local estimates are mixed, and we do not screen local estimates that are known to be suspicious (predicted by the formal error covariance).

All the local estimates are then injected into the interpolation scheme. If a local inversion method was not deployed at global scale due to computation limitations, regional results are generalized to global scale to get as close to the nominal global interpolation case as possible. Fig. 8 shows the along-track roll signal simulated (red) from the pessimistic roll scenario (i.e., with modes as fast as 120 s), and the interpolated correction (orange) on a coastal transition. Input data from local estimates are shown as color dots, and the color code shows which method provides the input data. Note that each local inversion was performed by packets: along-track scenes or cross-over segments.

The final interpolated roll correction is significantly more accurate than local estimates: packets of local estimates can be biased (particularly visible on pink packets of dots from land crossovers), but the propagated/interpolated error is not. Indeed, the input covariance error C_{rr} from (10) accounts for scene-specific biases for certain inversion methods to minimize their impact. In other words, biases on local inversions are not a problem for the interpolation scheme as long as the risk is statistically predicted by the formal error matrix of each inversion method [E_{xx} from (4)].

Fig. 9 shows a map of the residual roll signal after the interpolation (difference between the simulated scenario and the estimated signal). The residual error for very low-frequency roll signals (>1 h) is nonexistent, and the more rapid modes (120 s or 800 km) present in the pessimistic case have small residuals: less than 0.05 arcseconds on ocean (i.e., less than 2 cm RMS on the outer edge of the swath), and 0.08 arcseconds RMS on land (i.e., less than 3.5 cm).

Note that sensitivity tests (not shown) showed that if the interpolation is performed while purposely not using crossovers between SWOT (KaRIN + Jason-class nadir instrument) and external pulse-limited altimeters (Jason-CS and Sentinel-3C), the global error on ocean increases by 40% (i.e., 0.07 arcseconds or 3.5 cm). Therefore, the better results obtained on ocean are partly due to the availability of more cross-calibration segments derived from traditional nadir altimeters (discussed in Section VI-A).

The interpolated correction performs significantly better than raw local estimates because the objective analysis builds upon them: the optimal propagation implicitly performs a screening/weighting process of suspicious local estimates, as well as a smoothing of noise (if the formal error of the first step warns about potential noise) and bias removal (if the formal error warns about potential biases).

D. Baseline Length

The uncorrected baseline length error simulated as an input is a Gaussian process correlated over 800 s, i.e., more than 5000 km with a standard deviation of 0.1 mm. As per Section I-D2, the consequent error on the topography is a standard deviation of about 4 cm on the outer edges of the swath (quadratic signature across track as shown by Fig. 6). Our knowledge of the variations of baseline length should be largely better than this level of error according to SWOT's

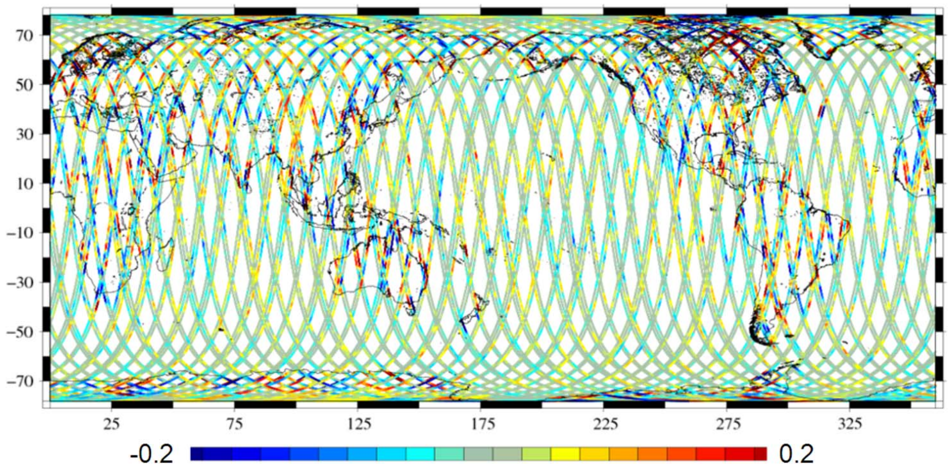

Fig. 9. Map of residual roll error after optimal interpolation. Unit: arcseconds.

TABLE IV
SYNTHESIS OF THE AVERAGE RESULTS OBTAINED ON LOCAL BASELINE ESTIMATION

Error used on input data	Ocean Crossover	Ocean Direct	Land Crossover	Land Direct	Ocean SWOTxJ3	Ocean SWOTxS3
All errors std (mm)	0.048	0.022	0.067	0.042	0.069	0.067
Roll error	0.027	~0	0.061	~0	x	x
Tropo error	0.056	0.010	0.061	0.019	x	x
Oceanic signal	0.059	0.049	x	x	x	x
Low frequency DEM	x	x	x	0.048	x	x
All errors and layover	x	x	0.100	0.064	x	x

requirements (see Section I-D-2). Like in the roll scenarios, we simulated additional higher frequency variations of the baseline length: 120 s, i.e., 800 km with a standard deviation of 0.05 mm RMS, i.e., a topography signature of 2 cm on the outer edges of the swath. However, we did not simulate high-frequency distortions nor thermal snaps which are beyond the scope of this paper (see Section I-C). Both the baseline roll and baseline length errors are concurrently simulated and estimated.

Like in previous sections, SWOT measurements are used as an input for local cross-calibration on small scenes or crossovers. The output of local inversions for various surfaces and methods is given in Table IV. The average residual error from both scenarios is 0.05 mm RMS on the baseline length, i.e., about 2 cm RMS on topography over cross-calibration zones. Table IV also gives some insight on the influence of various topography error terms of ε. On ocean, oceanic variability is a significant source of corruption (at least if intense mesoscale zones are included), whereas on land, the accuracy of the DEM first guess dominates. Assuming that the full extent of the wet troposphere residual error can corrupt SWOT's topography, it becomes a nontrivial source of corruption as well.

Generally speaking, the direct method is more accurate for δB, and the problem is easier to solve on land than on ocean. This is likely due to the signature of the baseline length error on crossovers (Fig. 6, right): the coherent bell-shaped structure induced by the difference of two arcs is harder to process because it can be interpreted as oceanic variability changes between both arcs (e.g., eddy intensification), particularly if the delta time is large. Conversely, the "gutter-shaped" quadratic signature is easier to detect with the direct method and long scenes, and notably on land where H_{real} is mostly static: only continental water surfaces have a dynamic component, and this topography change is unlikely to be misinterpreted as a coherent quadratic signature.

When local estimates are injected into the global optimal interpolation, the very slow modes disappear entirely as shown by Fig. 10: the residual baseline length signal is 0.002 mm (i.e., negligible for SWOT topography data). The residual signal for higher frequency modes (800 km or 120 s) is also very good with an average residual error of 0.035 mm on the baseline length, i.e., 1.5 cm on the topography of the outer edges of the swath. The end-to-end cross-calibration scheme has reduced the baseline length error by a factor of 3 (high-frequency modes) to 50 (very slow modes).

E. Synthesis

All the simulations we performed allow being very confident in the ability to control slowly varying baseline roll and baseline length errors in a purely empirical way on SWOT's Level 2 products. For very slow modes (e.g., orbital revolution, i.e., 1 h or more), the residual error observed is nonexistent when our technique is applied and [9] have shown that simpler algorithms (e.g., ocean crossovers only, least square inversions, spline propagation) could be efficient as well.

Moreover, the most complex cross-calibration scheme from Fig. 4 yields acceptable errors even in very pessimistic scenarios with respect to SWOT's mission requirements. The simulated input error we tried to reduce is largely beyond the

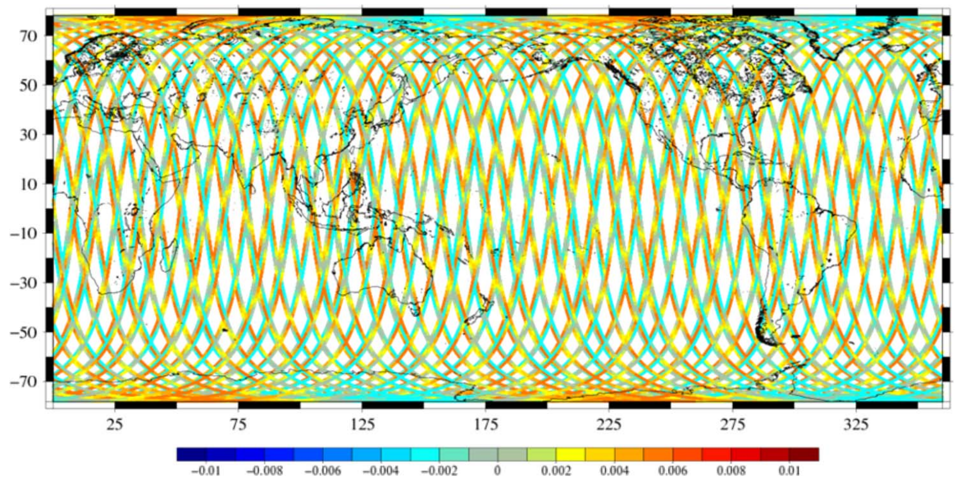

Fig. 10. Map of residual baseline error after optimal interpolation. Unit: meters.

current mission requirements both in terms of amplitude and frequencies.

Residual errors at the outer edges of the swaths are 1.5 to 2 cm RMS for exceptionally strong input errors (up to 70 cm if uncorrected). Because they are linear or quadratic signatures, the error RMS in the entire swath is smaller and largely compatible with SWOT's error requirement on height accuracy or slope accuracy. Moreover, the cross-calibration prototype used in these simulations is relatively complex, but it does not use all the local inversion methods from Section VI-E, so it is possible to envision better empirical cross-calibration algorithms by SWOT's launch.

VI. Discussion: General Cross-Calibration Findings and Considerations

This section addresses more general findings and considerations regarding empirical cross-calibration applied to SWOT measurements. Section VI-A discusses the complementarity between SWOT and traditional altimeters, Section VI-B deals with the sensitivity of these results to a wrong *a priori* knowledge given to the inverse methods; Section VI-C focuses on the specificities of SWOT's orbit, Section VI-D on observability problems. Lastly, Section VI-E outlines other cross-calibration techniques and their interest for SWOT.

A. Could SWOT Benefit From Traditional Altimetry?

By the time of SWOT's launch, at least one concurrent altimeter (namely Jason-CS) is expected to be in operations, and possibly two or three sensors (Sentinel-3C and HY-2C) or more (Jason-3, Sentinel-3B not decommissioned). These nadir-limited altimeters are useful for SWOT's cross-calibration:

A. Because merging their 1-D topography profiles in 2-D low-resolution maps provides a proxy H_{ref} of H_{real} to minimize the absorption of actual oceanographic signals in the empirical inversion. By removing a low-resolution sea surface height proxy before using the direct method [(2)], or crossovers [(8)], we ensure that actual mesoscale ocean topography features (e.g., eddies) are not misinterpreted as roll/baseline topography signatures (e.g., the bell-shaped feature from Fig. 6).

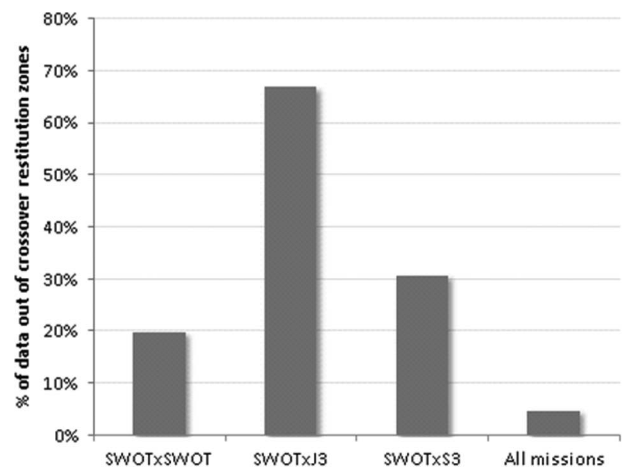

Fig. 11. Percentage of SWOT measurement out of cross-over calibration zones (i.e., not in the gray arrows from Figs. 2 and 3). Four cases are considered: SWOT/SWOT crossovers only, SWOT/Jason crossovers only, SWOT/Sentinel3 crossovers only, or the sum of all possible crossovers for SWOT.

B. Because they provide concurrent topography content on KaRIN x Nadir cross-over segments (and data sets that are not affected by KaRIN-specific errors). Therefore, nadir data provide a way to observe directly the roll/length errors in cross-over differences [see Sections II-A and III-B1 and (7)].

The length of the cross-calibration segments between KaRIN and pulse-limited altimeters change with latitude as a function of the cross-over angle between the two ground tracks (see SWOT orbit in Section VI-C). For the orbits used (SWOT, Jason, Sentinel), cross-calibration zones range from 50 to 250 km. Assuming that KaRIN can be cross-calibrated with three noncoordinated Nadir altimeters, cross-over zones are ubiquitous on ocean (and dense on large rivers and lakes).

Fig. 11 gives an overview of the percentage of SWOT data that would be out of cross-calibration zones for various configurations. With SWOT alone, it is already possible to provide local error estimates from crossovers over 80% of the data (assuming that KaRIN plus a Jason-class pulse-limited altimeter are onboard). If all crossovers are used (i.e., SWOT/SWOT + SWOT/Jason + SWOT/Sentinel), then Fig. 11 shows that more than 95% of the swath is directly observed by local cross-calibration methods. The size of "cross-calibration gaps" (i.e., the distance from one crossover to the next one) is approximately 125 km in average when only SWOT is considered, and less than 50 km when the two concurrent nadir altimeters are used.

Lastly, in addition to cross-calibration coverage, using more concurrent sensors allows to envision more complex cross-calibration schemes. Instead of having only one cross-over estimate per SWOT measurement time, exploiting multiple missions gives access to multiple observations for each time step of SWOT data (i.e., each image "cross-track line"). We therefore increase the amount of observations for the along-track interpolation. The more input data, the better the final accuracy notably for higher frequencies of R and δB. This is why the roll correction is 40% more efficient on ocean when external nadir altimeters are used (Section V-C).

B. Errors in the Statistical Problem Description

Various sensitivity tests were carried out to infer the changes in local inversion performance when the *a priori* knowledge is inaccurate, i.e., when the C_{xx}, C_{vv}, C_{rr} matrices are erroneously set up. To properly constrain SWOT's empirical cross-calibration, it is much more important to know the signal scales than the signal amplitude or variance.

When the amplitude or variance of an *a priori* error budget is wrongly defined, but still with a realistic order of magnitude, R and δB are not much affected: oceanic variability is the most sensitive parameter and a factor of two in the variance error budget results in about 8% of additional residual error of R and δB after cross-calibration. However, a wrong input variance budget has a much larger impact on the output formal error: the formal or predicted error on the output field can be wrong by 20% to 25%.

When an error or signal is assumed to be correlated, the realism of the correlation model used is important. For instance, if the oceanic variability is considered, cross-over differences only contain the high-frequency and small-scale signals δH_{HF}, because a large fraction of the full mesoscale variability is cancelled in the cross-over difference. The typical scales of the residual signal (observed on high-pass filtered of sea surface height fields) are 50 km and less than 5 to 7 days. These are the correlation scales that should be used in C_{vv}. However, if C_{vv} is created with the average decorrelation scales of the full mesoscale variability (150 km and 15 days), the estimated values of R and δB can be changed by more than 20%, and the formal error can be changed by 30% or more (notably at the outer edges of the local inversion scenes and crossovers).

C. Specificities of the SWOT Orbit

The satellite orbit has a strong impact on cross-calibration coverage and performance. The ground track (i.e., orbital parameters) controls the shape, direction and size of cross-calibration zones: Fig. 12 gives a simplified overview of the influence of the ground track direction on the size of the cross-over scene. When both swaths are nearly perpendicular (a), the scene is short with few observations, but when both swaths are almost parallel (b), the cross-calibration can be performed on a long segment exploiting twice as many observations. Fig. 13(a) (blue curve) gives an overview of the variations of the cross-calibration scene changes as a function of latitude, and Fig. 13(b) (blue curve) gives the origin of this variation: a change in the cross-over angle created by the geometry of SWOT's ground track.

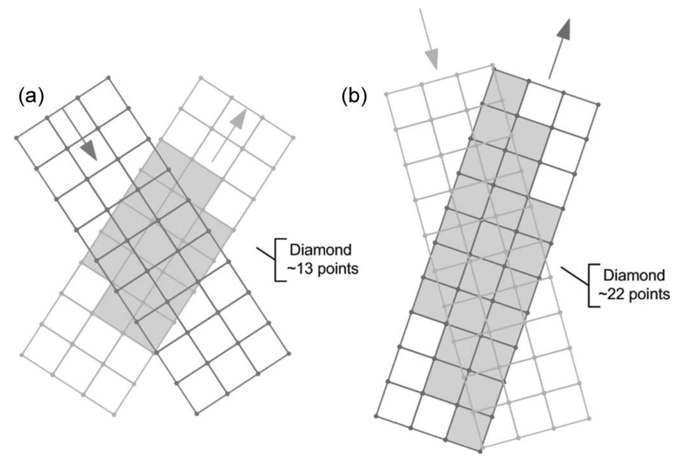

Fig. 12. Modification of the cross-calibration zone geometry with different cross-over angles (length and number of pixels in a simplified low-resolution swath).

Moreover, the satellite orbit also controls the temporal sampling (see Section I-B) and therefore the temporal distribution of cross-calibration observations. Fig. 14 shows a map of the temporal differences between the ascending and descending arcs on SWOT/SWOT crossovers (limited to δT of ± 10 days). The shorter the cross-over delta time, the better H_{real} and ε cancel out in the difference performed in (7) and (8). The map exhibits coherent lines of delta times: all crossovers located at a given latitude have the same delta time. Consequently, some latitudes are favorable to cross-calibration (light blue/green dots on Fig. 14); while other latitude bands will be slightly more problematic if only SWOT data are used (red/purple dots on Fig. 14).

Exploiting multiple inversion methods and two concurrent Nadir altimeters is largely able to mitigate this effect. Fig. 15 shows a map of the along-track segments where each inversion is performed, and the black circles highlight coverage weaknesses: subplot (a) is for the direct method with notable gaps in zones with strong mesoscale activity, subplot (b) is for SWOT/SWOT crossovers with gaps at specific latitude bands derived from Fig. 14, subplots (c) and (d) are for SWOT/Jason and SWOT/Sentinel crossovers (pessimistically considered unavailable over land, including on fresh water bodies). Each method and data source alone would suffer from coverage gaps and systematic local performance losses, but the sum of all the estimates mitigates each weakness, hence additional benefits from using traditional altimetry (Section VI-A).

D. Observability and Error Separation

The major sources of residual errors in local estimates from Section III are observability issues. This section provides various illustrations to highlight the limits of empirical cross-calibration.

1) Direct Method: Fig. 16 explains the observability phenomenon for the direct method, in a simplified case. Fig. 16(a) shows an ideal SWOT swath and the along-track segment where

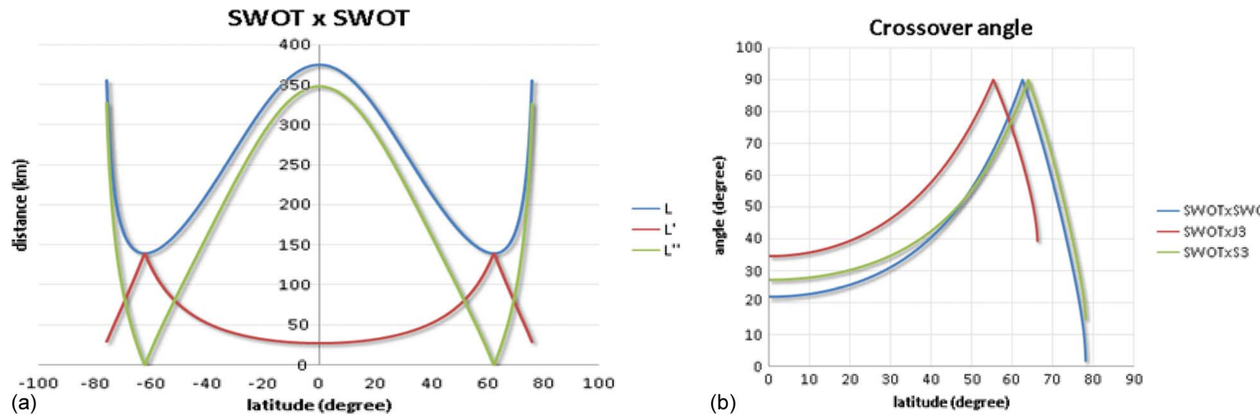

Fig. 13. Length (kilometers) of the SWOT/SWOT cross-calibration segments as a function of latitude (a) and SWOT cross-over angles in ° (b). L is the overall cross-over calibration zone, L' is the Karin/Karin cross-calibration zone (limited to perfect observations, i.e., light gray areas of Fig. 17), and L'' is the Karin/Nadir cross-calibration zone (see Fig. 2). The singular point at 62° is due to perpendicular crossovers between SWOT ground tracks.

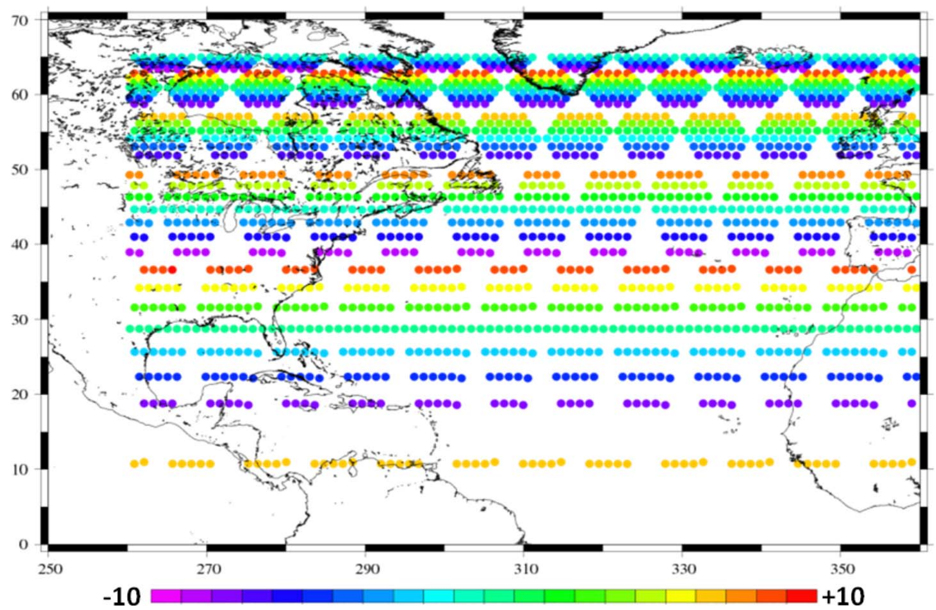

Fig. 14. SWOT cross-over delta time in days, i.e., temporal difference between the ascending and the descending arcs. The coverage is limited to crossovers with a δT inferior to 10 days.

empirical cross-calibration will be performed. Fig. 16(b) shows a degraded coverage on this data set. In the middle of the scene, the swath is incomplete and missing almost the entire left 1/2 swath. This can be due to actual data gaps or to edited or suspicious data: known DEM error, oceanic variability too large, change of surface type and instrumental behavior, uncontrolled layover effects in the area, etc. Fig. 16(c) thus artificially defines three zones: light gray where the observation is perfect and not affected by the data gap, dark gray where observation is minimal and limited to the right 1/2 swath, and the intermediate configuration with a slightly degraded situation. In practice, the change is continuous.

Fig. 16(d) shows what happens on the cross-track direction when actual topography features are added to the linear roll signature. In this ideal case, it is easy to visually or numerically separate the roll signature (linear) from the actual topography content (not linear). However, when the observation is not complete, and more precisely limited to one 1/2 swath (or less), then it becomes difficult or impossible to separate a partial linear signature from actual topography. The observation needed is missing, the error is no longer spectrally separable from the signal, and a misleading apparent roll value is given instead, like in Fig. 16(e). If the erroneous raw apparent roll is used "as is," the topography signal gets corrected from the wrong cross-track slope, thus removing true topography features.

If local estimates are injected into the along-track interpolation, local errors and discrepancies are largely mitigated. Indeed, the formal error estimate E_{xx} [(4)] provided along with the erroneous estimate is able to discriminate trustworthy roll estimates [light gray in Fig. 16(c)] from suspicious ones [dark gray in Fig. 16(c)]. The formal error is implicitly used in the along-track objective analysis from Section IV [matrix Crr from (10)], either to down weight suspicious input observations R_{est}, or to edit them out entirely.

2) Cross-Over Method: The observability limitation is also present in KaRIN/KaRIN crossovers as shown in Fig. 17.

Cross-over diamonds exhibit three zones ranging from light gray to dark gray like in Fig. 16(c). Although the roll/length errors of each arc are estimated concurrently, let us firstly assume that only the ascending arc (plain line) is corrected. The

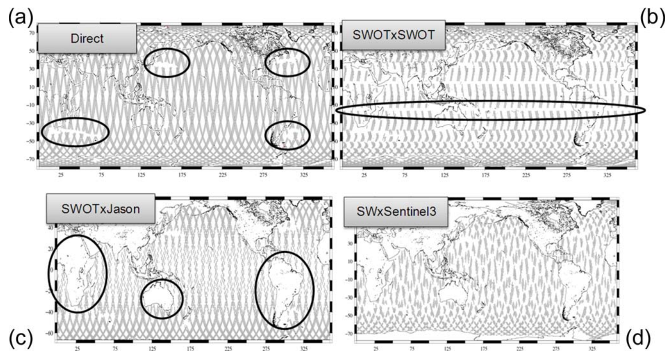

Fig. 15. Global coverage of the along-track cross-calibration segments [as defined in Figs. 2 and 3(b)] for various inversion techniques and references: the direct method based on a prior*a priori* knowledge from a DEM or MSS (a), crossovers between concurrent SWOT swaths (b), crossovers with a pulse-limited altimeter flying on the Jason orbit (c), and crossovers with a pulse-limited altimeter flying on a Sentinel-3 orbit (d). Black circle highlights the systematic gaps specifically associated with one method or reference.

descending arc (dashed line) is only given in Fig. 17 to explain the geometry of the scene. To correct for R and δB, topography differences from both swaths are used. Hence, the input data of local inversions are limited to measurements located in each of the four small diamonds, or four segments (see Section II-A and Fig. 3). Like in Fig. 16(b), limiting the input observations [Y from (8)] to a partial swath of the ascending arc degrades the observability and increases the residual error.

The worst case is located at the upper and lower edges of the cross-over diamond because only a small fraction of 1/2 swath can be used (the rest is not overlapping with the descending arc). In this configuration, the inversion becomes as difficult like in Fig. 16(e). Conversely, in light gray areas (center of the cross-over zone), local topography observations are either symmetrical (i.e., each 1/2 swath is fully contained in the large diamond and thus usable as a cross-over difference) or exploiting information from the nadir track of the opposite arc. In this configuration, the inversion can be done normally like in Fig. 16(d).

The descending arc has its own light/dark gray zones. Their geometry is defined by the same rules so the observability zones of the descending arc are symmetrical to the light/dark zones of the ascending arc (center of the diamond are trustworthy, outer edges are unreliable).

The consequence of this phenomenon is illustrated on actual data by Fig. 7(a): while the roll estimate is nearly perfect in the center of the along-track segment, i.e., the center of the crossover, outer edges exhibit increasing antisymmetrical errors due to observability problems. Ocean features have moved between the measurement time of each arc, thus creating residual topography differences [δH_{hf} in (8)]. In the center of the crossover, they can be separated from actual a roll signatures (Fig. 5, right) with matrices C_{xx} and C_{vv} from (3) [like in Fig. 16(d)] whereas on the outer edges, it is not possible [Fig. 16(e)]. Oceanic variability is absorbed by the empirical method because the spectral separation premise from Section II-A is not met entirely. Fortunately, the formal error (i.e., error predicted) given by the optimal inversion is consistent with the observed error [Fig. 7(b)]. In other words, one can predict observability errors.

Moreover, although a long along-track segment (dark gray arrow in Fig. 3) can be obtained from each crossover, the performance of the local inversion is not homogeneous in the scene. For very low-frequency signals (800 s or more), this is not an issue because the matrix C_{xx} (or simple linear adjustments) can constrain the problem and limit the negative influence of dark gray areas. However, for higher frequencies (less than 100 s), good local empirical estimates are limited to the light gray area (symmetrical observation, or visibility of the opposite Nadir profile).

In a conservative approach, the values used in Fig. 13(a) describe the light gray area from Fig. 17, (i.e., limited to trustworthy estimates of R and δB): the length L of each cross-calibration segment given on the blue curve is obtained as the maximum of L' in red (symmetrical KaRIN/KaRIN observations within the diamond) and L'' in green (visibility of the opposite nadir track). The singular point visible at latitudes of about 62° is created by the presence of orthogonal crossovers: the opposite Nadir profile can barely be used except on a single SWOT measurement time, but the KaRIN/KaRIN symmetrical zones are the largest because crossovers are square shaped instead of diamond shaped.

Fig. 13(b) shows that using different orbits (e.g., Jason-like) changes the geometry of the multimission crossovers, and the latitude of singular points, thus homogenizing the cross-calibration capability at global scale, hence the benefits of merging inputs from different altimeter orbits to improve SWOT's accuracy on ocean (Section VI-A).

3) Separating R and δB: Sections VI-D1 and VI-D2 showed that observability limitations are a problem if H_{real} is erroneously interpreted and absorbed as R and δB, thus empirically "deleting" actual topography content from SWOT images. However, a second effect involves the difficulty to separate R and δB or any other error term to be estimated (e.g., orbit error residuals or biases between SWOT's Jason-class altimeter and KaRIN).

Fig. 18 shows this point like Fig. 16(d) and (e). Being able to separate the linear roll signature and the quadratic baseline signature is simple when the cross-calibration is performed on an ideal and complete observation topography data set [represented by the bold black line on Fig. 18(a)]. However, when the input topography data set is very partial [bold black segment on Fig. 18(b)], it is difficult to separate both signatures because the observation is spatially limited. The quadratic topography signature can be erroneously interpreted as an apparent roll slope. The ideal case of Fig. 18(a) is associated with the light gray zones of Figs. 16 and 17, and the degraded case of Fig. 18(b) is associated with the dark gray zones.

While this effect is present in the results from Section V, it is not critical from a cross-calibration point of view. SWOT's topography is corrected as an apparent R linear signature instead as a quadratic δB signature. An error is made because a linear correction model is used instead of a quadratic one. Yet, because these models are used only wherever they were adjusted, the error made is largely inferior to the uncorrected signal: the local interpretation error (linear versus quadratic) is inferior to 1 cm on the outer 20 km of the swath.

Like all observability errors, this knock-on error (i.e., and error stemming from the confusion between baseline length and baseline roll signatures) can be taken into account in the interpolation scheme if necessary (not done in the simulations from Section V): during the 1-D optimal interpolation from

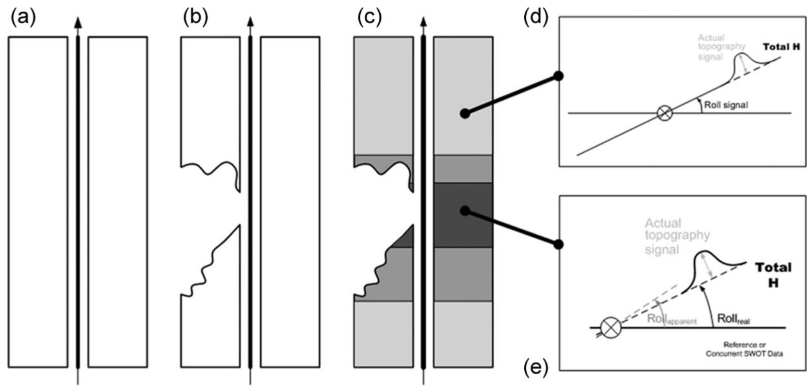

Fig. 16. Overview of the observability limitation from a partial swath and the direct method. Subplot (a) shows the SWOT swath geometry in an ideal case (i.e., gapless), and subplot (b) shows a case of missing or erroneous data (e.g., DEM not reliable for cross-calibration). Although the roll signature can generally be separated from actual topography information when the swath is complete (d), a limited topography observation (partial swath) can degrade the roll estimate (e).

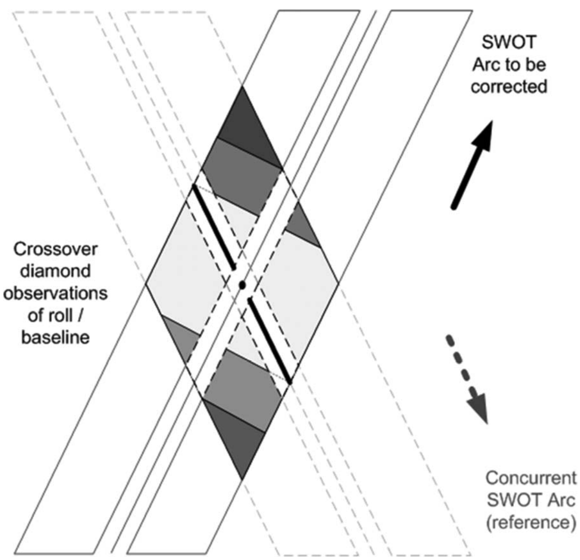

Fig. 17. Overview of the observability limitation from SWOT x SWOT crossovers. If one swath is to be corrected using information from a concurrent arc, some sections benefit from a complete overlap (both the left and right 1/2 swaths are overlapping the opposite arc, or the opposite Nadir measurement), and other sections only have a very partial overlap with the reference SWOT data set. This partial overlap is equivalent to the degraded sample from Fig. 16. Although the roll signature of both SWOT swaths can generally be separated from actual topography information wherever the overlap is complete as in Fig. 16(d), a limited topography observation (concurrent swath only partially overlapping and/or without opposite Nadir visibility) can degrade the roll estimate as in Fig. 16(e).

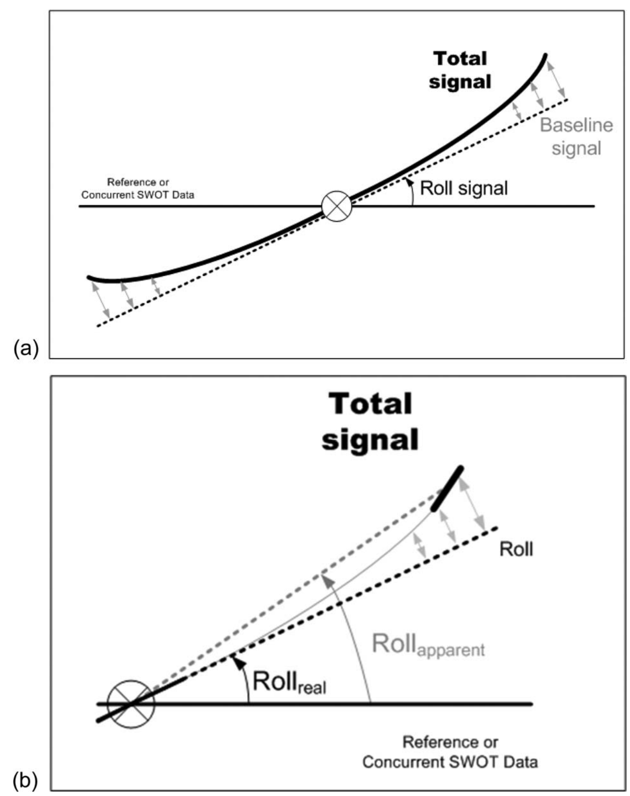

Fig. 18. Observability and separability of the roll and baseline signals. The ideal case of subplot (a) is associated with light gray zones of Figs. 16 and 17, and the degraded case of subplot (b) is associated with dark gray zones of the same figures.

Section IV, it is possible to perform a dual $[R, \delta B]$ propagation instead of separate ones, and to constrain a non-null correlation of local values of R_{est} and δB_{est} in Crr wherever local inversion is done with limited observability. Adding this correlation can theoretically provide additional information to the along-track global inversion and mitigate the corruption from one cross-calibrated parameter by the others.

E. Other Cross-Calibration Techniques and Perspectives

In addition to the direct and cross-over techniques used in this paper, other methods can be used to minimize the influence ε and H_{real} in local error estimates. This section outlines their specificities and interest.

The so-called "collinear" technique is derived from Labroue *et al.* (2008). It uses the same satellite pass from consecutive cycles. A simple difference cancels out any stationary ε and H_{real} signals (between consecutive cycles). This technique is interesting for short repeat cycles and notably for the 3-day Cal/Val phase envisioned at the beginning of SWOT's life: most of the H_{real} signal (e.g., medium to large mesoscale on ocean) would cancel out with a 3-day difference. The advantage of this method is that it can be used anywhere along the SWOT track, as opposed to geographically limited cross-over zones. However, for the 22-day orbit, this approach is interesting only on land (to cancel out static DEM topography) because the variations of fresh water levels and ocean structures have temporal decorrelation scales shorter than SWOT's repeat cycle.

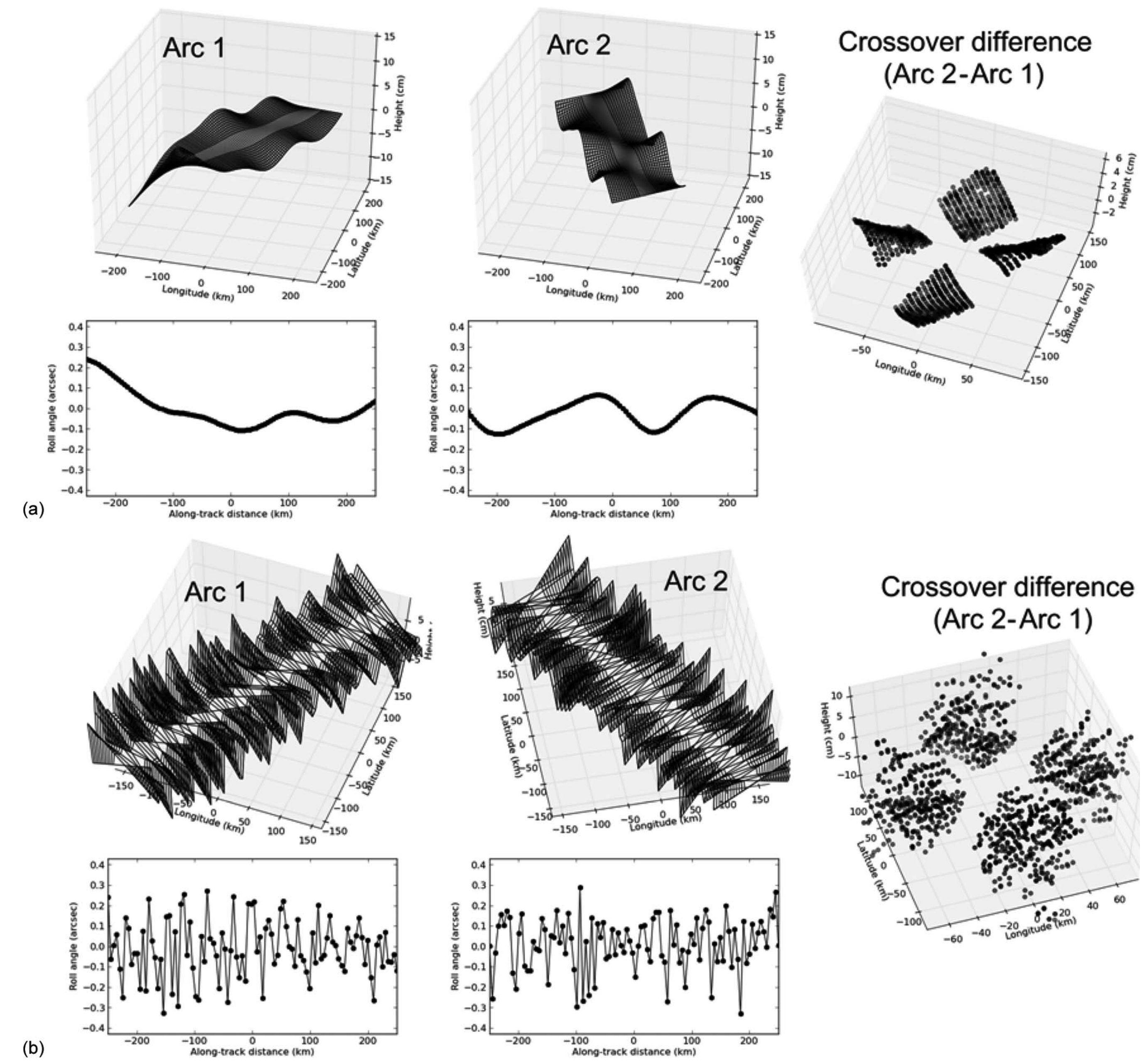

Fig. 19. Roll error signatures for two along-track decorrelation scales. Conceptual impact of the roll angle (bottom) on the KaRIN's topography (top) for two crossing swaths (left and middle), and residual topography difference visible on cross-over observations (right). Plate a shows a 200-km ($\sim$30 s) along-track decorrelation scale, and plate b shows a random process (no along-track correlation).

The "neighbor" technique uses a difference between adjoining swaths because they overlap. The 22-day orbit of SWOT also has a 3-day subcycle: adjoining SWOT passes are separated by only 3 days. Consequently, when the outer edges of adjoining swaths overlap enough (about 50% at midlatitudes), it is possible to apply the same inversion technique as on KaRIN x KaRIN crossovers: the difference of topography information from adjoining passes gives a direct access to the difference of the error signatures. This benefit is amplified by their shape (linear, quadratic): the error is observed wherever the signature is maximal (swaths overlap on their outer edges). If one arc (time t) is corrected using overlaps in the eastern 1/2 swath ($t - 3$ days) and in the western 1/2 swath ($t + 3$ days), the roll/baseline observation is symmetrical [Fig. 16(d)] and not prone to observability errors from Section VI-D. This method gives a quasiglobal cross-calibration capability. Contrary to the "collinear" method, this technique is primarily interesting for the 22-day orbit, and it is not applicable for short repeat cycles (e.g., 3-day CalVal phase) because adjoining swaths rarely overlap.

Exploiting additional methods is not necessary in this paper because our input errors are slowly varying (e.g., flexible mast and orbital oscillations). However, Fig. 19 shows that if the along-track (i.e., temporal) correlation decreases (e.g., caused by mechanical vibrations, or rigid baseline), the topographic signature becomes not only more problematic from a spectral point of view (e.g., overlap with the submesoscale spectrum where SWOT's error budget is the most stringent), but also more difficult to measure both along-track (direct method) and on crossovers: the signal is barely constant on any scene or crossover, so observability issues from Section VI-D become a dominant problem. In the case of purely random "roll signatures" [Fig. 19(b)], it is visually impossible to extract the roll signal from the cross-over difference. In this case, the numerical inversion is possible but strongly degraded. To correct this type of high-frequency errors, it is necessary to use all local inversion methods concurrently, but also to use external data and external nadir altimetry missions. In this case, for each line of the KaRIN image (i.e., each random "roll" value), one would get up to seven roll estimates (four types of crossovers, one direct method, one neighbor method, and one collinear method) with different strengths and weaknesses, thus improving the observation of higher frequency errors.

VII. Conclusion

Empirical cross-calibration of geographically coherent errors from KaRIN measurements has been prototyped from end to end in a framework exploiting multiple inversion techniques, and input data. Applied to the baseline roll and baseline length errors, the prototype is able to mitigate even very pessimistic input error scenarios (up to 70 cm RMS if left uncorrected) to acceptable levels. Residual topography errors on the outer edges of the swaths are 1.5 to 2 cm RMS for exceptionally strong and rapid input errors with respect to SWOT's mission requirements.

The correction is performed in a two-step approach: local inversions on along-track scenes or crossovers (on land and on ocean), and then a global propagation taking local estimates as an input. Exploiting pulse-limited altimeters notably provides a large amount of additional observations in areas where SWOT alone would be more difficult to calibrate. Concerning the inversion itself, optimal inverse methods allow using *a priori* knowledge of the problem to be solved (e.g., statistical description of the signal and errors, dominant normal modes for oscillation/deformation, etc.) to improve the output correction and to provide a trustworthy description of the error made on the estimation.

While low-frequency errors (800 s or more) are easy to cross-calibrate, exploiting external data sets and *a priori* knowledge is a needed addition when the problem is more complex (e.g., modes of about 120 s, uncorrected error amplitudes an order of magnitude higher than the signal itself). Our method provides better results when the problem is statistically well-described (modes, signatures, variances, correlation scales), but approximate knowledge is sufficient. To that extent, our results on a first prototype and end-to-end simulations allow being very optimistic with respect to the control of geographically or temporally coherent errors on SWOT products.

More generally, this approach can be used to empirically cross-calibrate residual errors on other types of wide swath topography data (e.g., near-nadir KaRIN data) but also to minimize errors from any type of wide swath sensor, if three premises are met: 1) the errors to minimize are geographically and/or temporally coherent (or linked to other measured parameters); 2) they can be modeled (analytical or nonparametric models); and 3) it is possible to spectrally separate the signal of interest from the error signatures (e.g., using measurement overlaps).

Acknowledgment

This work was performed in the framework of CNES' Research & Technology program, initially to support early processing prototypes for the so-called Wide-Swath Ocean Altimeter and more recently as a risk reduction initiative for the SWOT.

The authors would like to thank E. Rodríguez and V. Enjolras for discussions on instrumental capabilities and earlier work on cross-calibration methods, F. Briol for providing many tools to better observe the sampling of cross-calibration zones, MERCATOR-France for providing the OGCM data used to perform the global simulations, and CGIAR-CSI for providing the SRTM-derived D.E.M used to simulate land topography.

References

[1] M. Ablain, S. Philipps, N. Picot, and E. Bronner, "Jason2 Global statistical assessment and cross-calibration with Jason1," *Marine Geodesy*, vol. 33, no. S1, pp. –185, 2010.
[2] AVISO, *Cal/Val and Cross-Calibration Annual Reports*, 2010. [Online]. Available: http://www.aviso.oceanobs.com/es/calval/systematic-calval/index.html
[3] AVISO, *SSALTO/DUACS User Handbook: (M)SLA and (M)ADT Near-Real Time and Delayed Time Products*, CNES document SALP-MU-P-EA-21065-CLS, 2010. [Online]. Available: http://www.aviso.oceanobs.com/en/data/tools/aviso-user-handbooks/index.html
[4] P. Berry, Garlick, and Smith, "Near-global validation of the SRTM DEM using satellite radar altimetry," *Remote Sens. Environ.*, vol. 106, no. 1, pp. 17–27, 2007.
[5] F. P. Bretherton, R. E. Davis, and C. B. Fandry, "A technique for objective analysis and design of oceanographic experiment applied to MODE-73," *Deep-Sea Res.*, vol. 23, pp. 559–582, 1976.
[6] G. Dibarboure, M. Ablain, S. Philipps, P. Y. Le Traon, and J. C. Souyris, "Roll error reduction on a wide-swath altimeter," presented at the Ocean Surface Topography Science Team meeting, 2007. [Online]. Available: http://www.aviso.oceanobs.com/fileadmin/documents/OSTST/2007/dibarboure_WSARollError.pdf
[7] M. Dibarboure, M.-I. Pujol, F. Briol, P. Y. Le Traon, G. Larnicol, N. Picot, F. Mertz, and M. Ablain, "Jason-2 in DUACS: Updated system description, first tandem results and impact on processing and products," *Mar. Geod.*, vol. 34, no. 3-4, pp. 214–241, 2011, DOI: 10.1080/01490419.2011.584826.
[8] M. Durand, L. Fu, D. Lettenmaier, D. Alsdorf, E. Rodriguez, and D. Esteban-Fernandez (2010, May). The surface water and ocean topography mission: Observing terrestrial surface water and oceanic submesoscale eddies. *Proc. IEEE* [Online]. *98(5)*, pp. 766–779. Available: DOI:10.1109/JPROC.2010.2043031
[9] V. Enjolras, P. Vincent, J. C. Souyris, E. Rodriguez, L. Phallipou, and A. Cazenave, "Performances study of interferometric radar altimeters: From the instrument to the global mission," *Sensors*, vol. 6, no. 3, pp. 164–192, Mar. 2006.
[10] Y. Faugere, J. Dorandeu, F. Lefevre, N. Picot, and P. Femenias, "Envisat ocean altimetry performance assessment and cross-calibration," *Sensors*, vol. 6, no. 3, pp. 100–130, Mar. 2006.
[11] L. L. Fu and E. Rodriguez, "High-resolution measurement of ocean surface topography by radar interferometry for oceanographic and geophysical applications," in *The State of the Planet: Frontiers and Challenges in Geophysics*, vol. 19, *IUGG Geophysical Monograph*. Washington, DC: AGU, 2004, pp. 209–224.
[12] LEGOS, *Lakes, Rivers and Wetlands Water Levels From Satellite Altimetry, The Hydroweb Database*, 2011. [Online]. Available: http://www.legos.obs-mip.fr/en/soa/hydrologie/hydroweb/
[13] P. Y. Le Traon and F. Ogor, "ERS-1/2 orbit improvement using TOPEX/POSEIDON the 2 cm challenge," *J. Geophys. Res.*, vol. 103, no. C4, pp. 8045–8057, Apr. 1998.
[14] P. Y. Le Traon, F. Nadal, and N. Ducet, "An improved mapping method of multisatellite altimeter data," *J. Atmos. Ocean. Technol.*, vol. 15, no. 2, pp. 522–533, Apr. 1998.
[15] P. Y. Le Traon and G. Dibarboure, "Mesoscale mapping capabilities from multiple altimeter missions," *J. Atmos. Ocean. Technol.*, vol. 16, no. 9, pp. 1208–1223, Sep. 1999.

[16] P. Y. Le Traon and G. Dibarboure, "Velocity mapping capabilities of present and future altimeter missions: The role of high-frequency signals," *J. Atmos. Ocean. Technol.*, vol. 19, no. 12, pp. 2077–2087, Dec. 2002.

[17] E. Rodriguez, C. S. Morris, and J. Belz, "A global assessment of the SRTM performance," *Photogram. Eng. Remote Sens.*, vol. 72, no. 3, pp. 249–260, Mar. 2006.

[18] Science Requirements Document E. Rodríguez, Surface Water and Ocean Topography Mission (SWOT)2009, Science Requirements Document.

[19] E. Rodriguez and D. Esteban-Fernandez, "The surface water and ocean topography mission (SWOT): The Ka-band Radar Interferometer (KaRIn) for water level measurements at all scales," in *Proc. SPIE*, 2010, p. 782 614.

[20] E. Rodríguez, "The surface water and ocean topography (SWOT) mission," presented at the Ocean Surface Topography Science Team meeting, 2010. [Online]. Available: http://www.aviso.oceanobs.com/fileadmin/documents/OSTST/2010/oral/22_Friday/afternoon/Rodriguez.pdf

[21] E. Rodríguez, *A New Approach for Wide-Swath Ocean Interferometery Noise Reduction*, 2010. submitted for publication.

[22] P. Rosen, S. Hensley, I. R. Joughin, F. K. Li, S. Madsen, E. Rodriguez, and R. Goldstin, "Synthetic aperture radar interferometry," *Proc. IEEE*, vol. 88, no. 3, pp. 333–382, Mar. 2000.

[23] P. Schaeffer, A. Ollivier, Y. Faugere, E. Bronner, and N. Picot, "The new CNES/CLS 2010 mean sea surface," in *Proc. Ocean Surf. Topography Sci. Team meeting*, 2010. [Online]. Available: http://www.aviso.oceanobs.com/fileadmin/documents/OSTST/2010/oral/19_Tuesday/Schaeffer.pdf

[24] C. K. Tai, "Geosat crossover analysis in the Tropical Pacific 1. Constrained sinusoidal crossover adjustment," *J. Geophys. Res.*, vol. 93, no. C9, pp. 10 621–10 629, 1988, doi: 10.1029/JC093iC09p10621.

[25] S. Labroue, M. Ablain, S. Philipps, and N. Tran, "Comparison of Jason-1 and Jason-2 Sea State Bias," presented at the Ocean Surface Topography Science Team meeting, 2008. [Online]. Available: http://www.aviso.oceanobs.com/fileadmin/documents/OSTST/2008/oral/labroue.pdf

Gerald Dibarboure received the engineering degree from the French Aeronautics and Space System Engineering School (ISAE/SupAero).

He joined Collecte Localisation Satellites (CLS) Toulouse in 1998 where he developed the multi-altimeter merging system DUACS (Developping Use of Altimetry for Climate Studies) producing the gridded ocean topography maps distributed by AVISO (Archivage Validation et Interpretation des données des Satellites Océanographiques). He has contributed to altimetry mission design, end-to-end performance analyses, and multimission sampling analyses (T/P tandem, AltiKa, Sentinel-3, Jason tandem, Jason CS, SWOT) as the Head of the Calibration, Validation, and Data Fusion department. He is currently the Technical Manager of CLS' Space Oceanography Division.

Sylvie Labroue received an engineer degree from Institut National des Sciences Appliquées at Toulouse, France, in 1998, with a specialization in applied mathematics.

She joined Collecte Localisation Satellites (CLS) in 1999 where she was involved in the verification phase of Jason and ESA's ENVISAT altimetry mission. Her research interests include empirical estimation methods such as nonparametric sea state bias, neural network algorithms developed for the ENVISAT radiometer (wet path delay correction) and the ESA's SMOS salinity mission (ocean salinity retrieval) and Level 3 altimetry multimission products [SSALTO DUACS (Developping Use of Altimetry for Climate Studies) system].

Michael Ablain received the engineering degree in applied mathematics from the Institut National des Sciences Appliquées, Toulouse, France.

He joined Collecte Localisation Satellites (CLS) in 1999 as a project engineer in charge of the Calibration and Validation of the TOPEX/Jason series. His research interests included the improvement mean sea level and climate data records, and the understanding of coherent altimetry errors. He is currently head of the Mission Performance and Climate department in CLS' Space Oceanography Division.

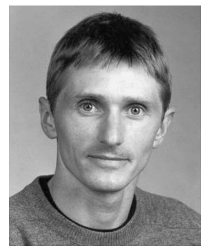

Roger Fjørtoft received the M.S degree in electronics from the Norwegian Institute of Technology, Trondheim, Norway, in 1993, and the Ph.D. degree in signal processing, image processing, and communications from the Institut National Polythechnique, Toulouse, France, in 1999.

He was a Senior Research Scientist at the Norwegian Computing Center in Oslo, from 2000 to 2003, and has since then been with the French Space Agency Centre National d'Etudes Spatiales in Toulouse, France. He is currently coordinating the activities related to synthetic aperture radar imagery in the Altimetry and Radar department (DCT/SI/AR).

Alain Mallet received the Ph.D. degree in microwave communications in 1996.

He joined the Microwave and Optical Communications Research Institute (IRCOM) in 1993. He worked on high efficiency amplifiers design methods. He joined the Toulouse Space Center (CNES) in 1999 and he's part of the radar and altimetry department. He is currently the CNES Payload Manager of the on-development Surface Water Ocean Topography mission.

Juliette Lambin graduated from the Ecole Polytechnique, Palaiseau, France, in 1997, then received the Ph.D. degree in geophysics from the Institute de Physique du Globe de Paris, France, in 2001.

From 2001 to 2005, she was a Posdoctoral Fellow at Californa Institute of Technology—Jet Propulsion Laboratory (Caltech/JPL), Pasadena. Her research interest included seismology, ionospheric sciences and remote sensing. In 2005, she joined Centre National d'Etudes Spatiales (CNES), Toulouse, France, working first as Mission engineer for altimetry missions. Since 2011, she is the program manager for ocean and cryosphere in the CNES Directorate for Startegy and Programmes.

Jean-Claude Souyris received the engineering degree in electronics from ENSEEIHT, Toulouse, France, in 1989 and the Ph.D. degree from the Université Paul Sabatier, Toulouse, France, in 1992.

He was a Visiting Scientist at the Center for Electromagnetic theory and applications at the Massachusetts Institute of Technology, Cambridge, in 1994. He joined the Centre National d'Etudes Spatiales, Toulouse, in 1997, where he is currently Head of the altimetry and radar department. He has authored or coauthored several articles dedicated to radar image processing, radar polarimetry, and radar altimetry.

Dr. Souyris served as the Technical Chairman of IGARSS'03, Toulouse, France.